

**Post-collisional magmatism and ore-forming systems in the
Menderes Massif: new constraints from the Miocene porphyry Mo–
Cu Pınarbaşı system, Gediz–Kütahya, Western Turkey**

Okan Delibaş^{1§}, Robert Moritz^{2*}, Massimo Chiaradia², David Selby³,
Alexey Ulianov⁴, Mustafa Kemal Revan⁵

¹: *Department of Geological Engineering, Hacettepe University, 06800, Beytepe-
Ankara, Turkey*

²: *Department of Earth Sciences, University of Geneva, Rue des Maraîchers 13,
1205 Geneva, Switzerland*

³: *Department of Earth Sciences, Durham University, Durham DH1 3LE,
United Kingdom*

⁴: *Institute of Earth Sciences, University of Lausanne, Géopolis, 1015, Lausanne,
Switzerland*

⁵: *General Directorate of Mineral Research and Exploration (MTA), 06800, Ankara,
Turkey*

*Corresponding author: Department of Earth Sciences, University of Geneva, Rue
des Maraîchers 13, 1205 Geneva, Switzerland. e-mail: robert.moritz@unige.ch

§ Deceased August 23, 2016

**Key Words: Post-collisional magmatism, Porphyry type mineralization, Ore-
forming systems, Re-Os molybdenite ages, Western Anatolia, Turkey**

1 **Abstract**

2 The Pınarbaşı Mo–Cu prospect is hosted within the Pınarbaşı intrusion, which is
3 exposed together with the NW–SE-trending Koyunoba, Eğrigöz, and Baklan plutons
4 along the northeastern border of the Menderes massif. The Pınarbaşı intrusion
5 predominantly comprises monzonite, porphyritic granite, and monzodiorite. All units
6 of the Pınarbaşı intrusion have sharp intrusive contacts with each other. The principal
7 mineralization style at the Pınarbaşı prospect is a porphyry-type Mo–Cu
8 mineralization hosted predominantly by monzonite and porphyritic granite. The
9 porphyry type Mo–Cu mineralization consists mostly of stockwork and NE- and EW-
10 striking sub-vertical quartz veins. Stockwork-type quartz veins hosted by the upper
11 parts of the porphyritic granite within the monzonite, are typically enriched in
12 chalcopyrite, molybdenite, pyrite, and limonite. The late NE- and EW-striking normal
13 faults cut the stockwork vein system and control the quartz–molybdenite–
14 chalcopyrite–sphalerite–fahlore–galena veins, as well as molybdenite–hematite-
15 bearing silicified zones.

16
17 Lithochemical and whole-rock radiogenic isotope data (Sr, Nd and Pb) of the host
18 rocks, together with Re–Os molybdenite ages (18.3 ± 0.1 Ma – 18.2 ± 0.1 Ma) reveal
19 that the monzonitic and granitic rocks of the Pınarbaşı intrusion were derived from an
20 enriched lithospheric mantle–lower crust during Oligo–Miocene post-collisional
21 magmatism. The lithospheric mantle was metasomatized by fluids and subducted
22 sediments, and the mantle-derived melts interacted with lower crust at 35–40km
23 depth. This mechanism explains the Mo and Cu enrichments of the Pınarbaşı
24 intrusion during back-arc magmatism. We conclude that the melt of the Pınarbaşı
25 intrusion could have rapidly ascended to mid-crustal levels, with only limited crustal

26 assimilation along major trans-lithospheric faults as a result of thinning of the middle
27 to upper crust during regional extension, and resulted in the development of
28 porphyry-style mineralization during the early Miocene (~18 Ma). The subsequent
29 exhumation history of the Mo–Cu-bearing Pınarbaşı intrusion is attributed to regional-
30 scale uplift, and further exhumation along detachment faults of the associated core
31 complexes during the middle to late Miocene.

32
33

34 **1. Introduction**

35 The Aegean Sea region belongs to the Tethys orogenic belt, and it is one of the
36 Cenozoic Mediterranean back-arc basins with the fastest rates of ongoing extension
37 on Earth, resulting in rapid thinning of the continental crust, detachment faulting,
38 exhumation of metamorphic domes, formation of supradetachment sedimentary
39 basins, and abundant post-orogenic magmatism (Bozkurt et al. 1993; Hetzel et al.
40 1995; Bozkurt and Park 1997; Ring et al. 1999, 2010; Koçyiğit et al. 2000; Doglioni et
41 al. 2002; Whitney and Bozkurt 2002; Bozkurt and Sözbilir 2004; Dilek et al. 2009;
42 Agostini et al. 2010). Ages of metamorphic dome exhumation and post-orogenic
43 magmatism exhibit a younging from north to south in the Aegean Sea region towards
44 the Hellenic trench (Jolivet et al. 2003; Jolivet and Brun 2010). This geodynamic
45 setting also provided a particularly favorable environment for the concentration of a
46 large variety of metal resources in the Earth's crust, as documented by the abundant
47 Cu, Au, and Pb-Zn deposits and prospects associated with the metamorphic domes
48 and/or post-orogenic magmatic provinces of the Aegean Sea region (Oygür 1997;
49 Arikas and Voudouris 1998; Oygür and Erler 2000; Marchev et al. 2005; Yigit, 2009;
50 Márton et al. 2010; Moritz et al. 2010, 2014; Voudouris et al. 2010; van Hinsbergen
51 and Schmid 2012; Kaiser-Rohrmeier et al. 2013; Sánchez et al. 2016; **Fig. 1**).

52

53 The Middle to Late Cenozoic Cu-Mo±Au-bearing porphyry systems within different
54 segments of the Tethys metallogenic belt, from the Aegean region through Anatolia
55 to the Lesser Caucasus, are closely associated with the post-collisional evolution of
56 the Tethys metallogenic belt (Konos Cu-Mo, Skouries Cu-Au-Mo, Pagoni Rachi Cu-
57 Mo-Ag-Au in Greece: [Voudouris et al. 2010; 2013a, b](#); Kisladag Au-Mo in Turkey:
58 [Sillitoe 2002, Yiğit 2009](#); Kerman Porphyry Cu-Mo belt in Iran: [Aghazadeh et al.](#)
59 [2015](#); Kadjaran Cu-Mo in Armenia: [Moritz et al. 2016, Rezeau et al. 2016](#)). The
60 Oligocene to Miocene, Greek Mo-Re-bearing porphyry systems in the Cenozoic
61 Mediterranean back-arc basin are closely linked to shoshonitic to calc-alkaline
62 magmatism that were produced by sub-continental lithospheric mantle–lower crust
63 interaction within a post-orogenic setting ([Kroll et al. 2002; Voudouris et al. 2010,](#)
64 [2013a, b](#)). In particular, the link with the regional tectono-magmatic evolution of
65 Eocene to Oligocene (~38 – 29 Ma) ore deposits/prospects of the oldest and
66 northernmost metamorphic dome province of the Aegean region in the Rhodope
67 Massif in Bulgaria and Greece has been addressed in detail ([Arikas and Voudouris](#)
68 [1998; Marchev et al. 2005; Márton et al. 2010; Moritz et al. 2010, 2014; Kaiser-](#)
69 [Rohrmeier et al. 2013](#)).

70

71 The northern zone of the Menderes Massif in Turkey is well endowed with numerous
72 mineral deposits/prospects and a large variety of commodities (**Fig. 1**), including
73 porphyry-type Mo–Cu–Au, skarn-type Fe and Pb–Zn, base metal and precious metal
74 epithermal deposits/prospects ([Gökce and Spiro 1994; Oygür and Eler 2000; Yiğit](#)
75 [2006, 2009; Delibaş et al. 2012a, b Oyman et al. 2013](#)). Some of the deposits and
76 prospects are spatially associated with post-collisional magmatic activity such as the

77 Ovacık Au-Ag deposit, with grabens at the Kurşunlu and Emirli Au-Ag-Sb-Hg-bearing
78 prospects, and the hanging- and footwalls of post-collisional detachment faults (**Fig.**
79 **1; Yiğit 2006**). Nevertheless, the link between post-collisional metallogenic evolution,
80 magmatism and extension remains poorly documented and constrained in the
81 Menderes Massif.

82
83 This study addresses the petrogenesis of ore-bearing felsic intrusions and the timing
84 of mineralization during post-orogenic evolution of the Menderes Massif in western
85 Anatolia. In this contribution, we report field observations from the Mo–Cu–Pınarbaşı
86 prospect, Re–Os molybdenite age data from the main mineralization stage,
87 lithochemical, and whole-rock radiogenic isotope data (Sr, Nd and Pb) from the
88 associated Oligo-Miocene granitic and monzonitic host rocks. Our aim is to constrain
89 the timing of mineralization, and its genetic link with the ore-associated magmatic
90 rocks and the geodynamic evolution of the Gediz–Pınarbaşı region.

91
92 **2. Regional Geology**

93 Following final accretion of the Gondwana-derived Sakarya block to the southern
94 Eurasian margin during the Late Cretaceous–Paleocene (**Şengör and Yılmaz 1981;**
95 **Okay and Tüysüz 1999**), western Anatolia underwent widespread extension from the
96 Oligo–Miocene to the present. Previous studies have concluded that the complex
97 extensional tectonic evolution has resulted in exhumation of metamorphic core
98 complexes, emplacement of felsic intrusions along shear zones, block faulting and
99 graben formation (**Bozkurt et al. 1993; Hetzel et al. 1995; Ring et al. 1999; Koçyiğit et**
100 **al. 2000**). Western Anatolia is segmented into several thrust-bounded metamorphic
101 zones, and includes from north to south: the Tavşanlı zone, the Afyon zone, and the

102 Menderes Massif (**Fig. 1, inset**; Şengör et al. 1984; Okay et al. 1998; Sherlock 1999;
103 Okay 2008; van Hinsbergen 2010). The oldest units in the region are the Menderes
104 Massif metamorphic rocks, which are tectonically overlain by the Lycian Nappes in
105 the south and the oceanic remnants of the Neo-Tethys in the north (Collins and
106 Robertson 1997; Bozkurt 2004). The northern and northeastern borders of the
107 Menderes Massif are crosscut by Cenozoic diorite, quartz diorite, monzonite,
108 granodiorite and granite. Three main magmatic episodes are recognized: 1) middle to
109 late Eocene, 2) Oligo–Miocene, and 3) middle-late Miocene to recent (Innocenti et al.
110 2005; Ring and Collins 2005; Hasözbek et al. 2010; Karaoğlu et al. 2010;
111 Altunkaynak et al. 2012a, b). Although their origin has been hotly debated, the
112 Eocene calc-alkaline felsic intrusions (55 – 38 Ma) are generally attributed to
113 subduction-related magmatism, partly sourced by metasomatised lithospheric mantle
114 during convergence and subsequent collision of the Sakarya and Anatolide–Tauride
115 blocks along the Izmir-Ankara subduction zone (IASZ) (Harris et al. 1994; Aldanmaz
116 et al. 2000; Koprubasi and Aldanmaz 2004; Altunkaynak et al. 2012b).

117
118 The duration of the second, Oligo–Miocene calc-alkaline to high-K calc-alkaline
119 magmatic cycle is well constrained between ~24.0 and 19.5 Ma with U-Pb zircon
120 ages from granite (Ring and Collins 2005; Hasözbek et al. 2010; Altunkaynak et al.
121 2012a) and ⁴⁰Ar/³⁹Ar (hornblende, biotite) ages record cooling ages of the Oligo-
122 Miocene granites that range between ~25 and 18 Ma, indicating fast cooling (Isik et
123 al. 2004; Aydoğan et al., 2008; Altunkaynak et al. 2012a). However, the origin of the
124 Oligo-Miocene magmatism remains open to question. Several models have been
125 proposed, including: 1) back-arc magmatism during southward roll-back and retreat,
126 as the African and Eurasian plates were converging, resulting in partial melting of the

127 lower crust during asthenospheric upwelling (Fytikas et al. 1984; Delaloye and Bingöl
128 2000; Pe-Piper and Piper 2001, 2007; Jolivet and Brun 2010; Ring et al. 2010;
129 Jolivet et al. 2015); 2) decompressional melting related to orogenic collapse of an
130 overthickened crust, at the late Oligocene-early Miocene transition (Seyitoglu et al.
131 1992; Seyitoglu 1997); and 3) post-collisional magmatism sourced by melting of
132 lithospheric mantle metasomatised during the preceding subduction stage, and
133 induced by asthenospheric upwelling. The latter is attributed to the Sakarya-
134 Taurides-Anatolides continent collision in the north and the subsequent extensional
135 stage related to subduction of the Aegean slab along the Hellenic arc (Aldanmaz et
136 al. 2000; Altunkaynak and Dilek 2006; Dilek et al. 2009). The Oligo–Miocene
137 magmatism accompanied a two-stage regional extension of western Anatolia,
138 starting with late Oligocene to early Miocene detachment faulting, such as the Simav
139 fault zone (**Fig. 1**), and late Oligocene to middle Miocene core complex exhumation
140 in the Menderes Massif, followed by graben formation with high-angle normal faulting
141 from middle to late Miocene (Pourteau et al. 2010; **Fig. 1**). The general agreement is
142 that the local granitic intrusions, named Eğrigöz, Alaçam and Koyunoba (**Fig. 1**), are
143 syn-tectonic, and that they intruded Paleozoic basement along the footwall of the
144 Simav detachment fault zone during early extension and metamorphic core
145 exhumation in the early Miocene (Isik et al. 2004; Dilek et al. 2009; Erkül 2010; Erkül
146 et al. 2013).

147
148 The last pulse of Cenozoic magmatism in the region consists of intraplate shoshonitic
149 to mildly alkaline and following OIB-type magmatism, during thinning of the Aegean–
150 Anatolian lithosphere in response to extension since the middle-late Miocene
151 (Doglioni et al. 2002; Innocenti et al. 2005; Agostini et al. 2007, 2010; Karaoğlu et al.

152 2010; Ersoy and Palmer 2013). The middle-late Miocene to early Pliocene pulse of
153 magmatism is mainly mildly alkaline to shoshonitic in nature and it shows a within-
154 plate character (Innocenti et al. 2005; Helvacı et al. 2009). On the other hand, the
155 early Pliocene to Quaternary phase of magmatism comprises sodic and potassic
156 magmatism and it displays clear OIB-type signatures (Alici et al. 2002; Innocenti et
157 al. 2005; Ersoy and Palmer 2013).

158

159 **3. Geological setting of the Pınarbaşı Mo–Cu prospect**

160 In the Gediz-Pınarbaşı region, the stratigraphic column comprises, from bottom to
161 top, Menderes Massif metamorphic rocks and low-temperature, high-pressure meta-
162 sedimentary units of the Afyon zone, followed by the Triassic–Jurassic Kırıkbudak
163 Formation composed of alternating sandstone, siltstone and limestone units with an
164 estimated thickness of 200 to 750 m, and a Late Triassic to Maastrichtian
165 dolomitized, platform-type limestone unit, known as the Budağan limestone with an
166 estimated thickness of 150 to 600 m (Akdeniz and Konak 1979; Okay et al. 1996;
167 Candan et al. 2005). These stratigraphic units are overthrust by Cretaceous to
168 Paleocene ophiolitic mélangé units, mostly comprising radiolarite, large limestone-
169 marble blocks, tuffite, and peridotite with a thickness of more than 750 m (Akdeniz
170 and Konak 1979). These rocks were intruded by early Miocene felsic rocks and their
171 sub-volcanic equivalents, including the Eğrigöz, Koyunoba, and Pınarbaşı intrusions
172 and the Simav volcanic rocks (Figs. 1 and 2a-b). The NW-trending Mo–Cu-bearing,
173 multiphase, calc-alkaline Pınarbaşı intrusion is crosscut by NW- and NS-striking
174 andesitic, dacitic, and aplitic dykes, and NE- and EW-striking Mo–Cu-bearing quartz
175 veins, whereas the limestone and mélangé units are crosscut by NW-trending
176 porphyry dikes (Delibaş et al. 2012a, b). The eastern zone of the mapped area is

177 dominated by Neogene and Quaternary volcano-sedimentary cover sequences (**Fig.**
178 **2a**).

179
180 The NW-trending active Simav and Kutahya fault zone next to the Pınarbaşı prospect
181 resulted in complex EW-, NW-, and NE-oriented block faulting (**Tokay and Doyuran**
182 **1979; Fig. 1, and inset in Fig. 2**). The Pınarbaşı intrusion is exposed on the
183 northwestern shoulder of the Yenidoğmuş–YeniGediz graben, and is controlled by
184 the NE-striking Eskigediz normal fault and the EW- to NW-oriented Şaphane normal
185 fault zone, which are associated with graben formation (**Gürboğa et al. 2013; inset in**
186 **Fig. 2**). The latter fault zone hosts the Şaphane deposit, which is the largest
187 epithermal alunite deposit of Turkey (**Mutlu et al. 2005**). Three generations of fault
188 systems have been recognized, including EW- and NW-striking normal faults, NE-
189 trending normal faults, dipping 70–80° to the NW (**Figs. 3a-b**), and late-stage NS-,
190 NW-, and NE-striking strike-slip local fault systems, which are largely developed
191 along the vertical contacts between the intrusion and limestone, and which crosscut
192 the hydrothermal alteration zones as well as earlier faults. The Pınarbaşı intrusion is
193 strongly mylonitized along its contact with the intensely silicified country rock (**Fig.**
194 **3c**). This masks the contact between the intrusion and its country rocks, and
195 conceals the late contact metamorphism along the margins of the intrusion (**Delibaş**
196 **et al. 2012a; Fig. 3c**). However, 0.5 to 1m-wide skarn zones containing garnet,
197 epidote, pyroxene, calcite, and magnetite are developed along the contacts of the
198 NW-trending porphyritic dykes crosscutting the limestone and the mélangé units (**Fig.**
199 **3d**).

200

201 The Pınarbaşı intrusion primarily comprises monzonite, porphyritic granite, and
202 monzodiorite (Delibaş et al. 2012a, b), which have sharp intrusive contacts with each
203 other (Fig. 3a). They contain roughly oval, fine-grained dioritic enclaves, with sharp
204 contacts with their host rocks. The largest intrusive body in the area is a fine- to
205 medium-grained monzonite with a largely equigranular texture. It predominantly
206 contains highly sericitized euhedral to subhedral plagioclase, subhedral K-feldspar,
207 subhedral to euhedral amphibole, biotite, pyroxene, minor quartz, and accessory
208 apatite. Epidote, calcite, chlorite, and sericite are alteration products of the main
209 mineral assemblage. A porphyritic granite cutting the monzonite is exposed in the
210 western part of the area (Fig. 3e). The intrusion of the porphyritic granite into the
211 monzonite resulted in the formation of an intrusion breccia (Delibaş et al. 2012a; Fig.
212 3f). The porphyritic granite is characterized by a more pronounced porphyritic
213 texture, consisting of plagioclase, biotite and K-feldspar phenocrysts within a fine-
214 grained matrix consisting of K-feldspar, plagioclase, biotite, amphibole, and quartz.
215 The monzonite and porphyritic granite are cut by bodies of dark-gray diorite and
216 monzodiorite with an equigranular to porphyritic texture. They have the same
217 mineralogical composition as the dioritic enclaves and generally consist of sericitized
218 plagioclase, amphibole, biotite, pyroxene, and minor quartz.

219

220 **4. The Pınarbaşı porphyry Mo–Cu-type prospect**

221 The Pınarbaşı Mo–Cu prospect is hosted by the Pınarbaşı intrusion, which is
222 exposed approximately 20 km southeast of the NW-trending active Simav fault zone.
223 The latter fault also hosts small to mid-scale high- and low-sulfidation epithermal and
224 Cu–Pb–Zn vein-type mineralization within the southern sector of the Afyon zone
225 (Oygür and Eler 2000; Fig 1). Based on drill hole data, the Cu and Mo contents of

226 the prospect vary between 374 and 34,800 ppm, and between 106 and 2,200 ppm,
227 respectively (Delibaş et al. 2012b).

228
229 The principal mineralization style at the Pınarbaşı prospect is a porphyry Mo–Cu type
230 mineralization hosted predominantly by monzonite and porphyritic granite. Field,
231 mineralogical, and lithogeochemical studies have also revealed the presence of Pb
232 and Zn enrichments up to 6.7 wt. % and 7700 ppm, respectively, within the Budağan
233 limestone (Oygür and Erler 2000; Delibaş et al. 2012a,b). In addition, Sb, Ag and Au
234 grades up to 1210 ppm, 12 ppm, and 1320 ppb, respectively, have been reported
235 within the silicified zones along the NW-striking, normal and strike-slip faults cutting
236 the limestone blocks of the ophiolitic mélange units and Sb, Ag, Au and Pb-rich
237 silicified zones within limestone blocks mainly show lattice textures (e.g., primary
238 bladed calcite, ghost bladed quartz, lattice bladed quartz), indicating a low-sulfidation
239 epithermal mineralization at relatively shallow depths (Delibaş et al. 2012b).

240
241 The porphyry-type Mo–Cu mineralization consists mostly of stockwork and NE- and
242 EW-striking sub-vertical quartz veins (Figs. 4a-b). Stockwork-type quartz veins within
243 the upper parts of the porphyritic granite typically contain chalcopyrite, molybdenite,
244 pyrite, and limonite. Late NE- and EW-striking normal faults, crosscutting the
245 stockwork mineralization, host quartz–molybdenite–chalcopyrite–sphalerite–
246 sulfosalts–galena veins and molybdenite–hematite-bearing silicified zones (Figs. 4c-
247 e). Potassic, sericitic, and argillic alterations are associated with the Mo–Cu
248 mineralization (Oygür and Erler 2000; Delibaş et al. 2012a, b). The local potassic
249 alteration zone within porphyritic granite of the Pınarbaşı intrusion is characterized by
250 small magnetite, biotite, and 1–5 cm thick K-feldspar veins (Figs. 5a-b). Sericitic

251 alteration is developed along the NE- and EW-striking ore-controlling faults, where
252 advanced argillic alteration is less intense, and it is dominated by sericite–muscovite,
253 pyrite, hematite, and small quartz veinlets (**Figs. 4b-c and 5c-d**). Sericitic alteration
254 grades locally into intense silicification, which contains small molybdenite-bearing
255 stockwork quartz veinlets. The intensity of silicification decreases away from the main
256 fault zones. Creamy to white advanced argillic alteration predominates at Pınarbaşı
257 and overprints the sericitic and potassic alterations. It primarily comprises
258 pyrophyllite, tabular alunite, fluorite, kaolinite, and illite (**Figs. 5e-f**). Jarosite,
259 smectite, and Fe-oxides along the late-stage normal and strike-slip faults are
260 interpreted as supergene alteration. Based on field observations, mineralization
261 styles, and alteration types, the Pınarbaşı prospect is interpreted as a porphyry-style
262 Mo–Cu mineralization, telescoped by low-sulfidation epithermal $Sb \pm Ag \pm Au \pm Pb$
263 mineralization and an intense advanced argillic alteration zone. Late supergene
264 alteration along younger fault zones overprints the earlier associations (**Oygür and**
265 **Erler 2000; Delibaş et al. 2012a**).

266

267 **5. Results**

268 Seventeen fresh rock samples from the Pınarbaşı granitoid were selected for whole-
269 rock lithochemistry analysis. Samples showing hydrothermal alteration effects
270 were removed and we used plutonic and subvolcanic rock samples revealing loss of
271 ignition (LOI) below 2.0 wt. % for petrologic interpretations to avoid potential
272 hydrothermal alteration effects. Twelve whole-rock powder samples were analyzed
273 for radiogenic isotopic compositions (Sr, Nd, Pb). Radiogenic isotope analyses were
274 conducted at the University of Geneva, Switzerland. We also report two new Re-Os
275 molybdenite ages from the main mineralization stage. The ^{187}Re and ^{187}Os

276 concentrations in molybdenite were determined in the Source Rock and Sulfide
277 Geochronology and Geochemistry Laboratory at the University of Durham, United
278 Kingdom. The details of the analytical techniques are summarized in **Online**
279 **Resource 1** and the major and trace element data of the Pınarbaşı intrusion are
280 listed in **Online Resources 2 and 3**.

281

282 *5.1. Whole-rock geochemistry of the Pınarbaşı intrusion*

283 The Pınarbaşı intrusive rocks range in composition from diorite–granodiorite to
284 monzonite with SiO₂ contents varying from 61 to 69 wt.% (**Fig. 6a**). All samples of the
285 Pınarbaşı intrusion straddle the boundary between alkaline and subalkaline series
286 and show a calc-alkaline trend on the AFM diagram (**Figs. 6a-b**). In addition, they
287 belong to the high-K calc-alkaline series on the K₂O vs SiO₂ classification diagram of
288 **Peccerillo and Taylor (1976; Fig. 6c)**. The Pınarbaşı samples are also transitional
289 metaluminous to peraluminous based on A/CNK (Al₂O₃/(CaO+Na₂O+K₂O)) values
290 varying from 0.9 to 1.2. The porphyritic granite members, i.e. the most evolved
291 samples, of the Pınarbaşı intrusion are mildly peraluminous, whereas the monzonite,
292 and enclave samples are predominantly metaluminous and display similarities with
293 western Aegean Oligo–Miocene felsic intrusions (**Fig. 6d**). On binary plots, the
294 samples show decreasing Al₂O₃, Fe₂O₃, MgO, CaO, TiO₂, and P₂O₅ contents with
295 increasing SiO₂ concentrations. Despite scattered variations, Sr, V, and Zr decrease
296 with increasing SiO₂, whereas Th and Ni display no marked correlation with
297 increasing SiO₂ (**see Online Resource 4**). All samples from the Pınarbaşı intrusion
298 display similar trace element patterns (**Fig. 7a**). They are enriched in large-ion
299 lithophile elements (LILEs; e.g., Th, K, Ba) and are depleted in high-field strength
300 elements (e.g., Nb, Ta, P, and Ti). Furthermore, they have trace element patterns

301 similar to those of the upper crust. The Pınarbaşı samples display a pronounced light
302 rare earth element (LREEs) enrichment with respect to middle (MREEs) and heavy
303 rare earth elements (HREEs) ($La_N/Yb_N = 10\text{--}36$, $La_N/Gd_N = 7.2\text{--}13$), with weak to
304 strong negative Eu anomalies ($Eu/Eu^* = 0.66\text{--}0.85$), and minor depletion in MREEs
305 ($Gd_N/Yb_N = 1.13\text{--}1.59$) (**Fig. 7b**).

306

307 *5.2. Whole-rock Sr, Nd, and Pb isotopic compositions*

308 The analytical techniques used in the study are summarized in **Online Resource 1**.

309 Sr, Nd, and Pb isotope ratios for whole-rock samples from Pınarbaşı (granitic and
310 monzonitic) are presented in **Tables 1 and 2**. The age-corrected initial Sr, Nd, and

311 Pb isotopic ratios were calculated for an age of 20 Ma, which is generally accepted

312 for Oligo–Miocene felsic intrusions in the region. The $^{87}Sr/^{86}Sr_{(i)}$ of the porphyritic
313 granite samples range from 0.70774 to 0.70923, whereas the initial Sr isotope ratios

314 of the monzonite and monzodiorite samples range from 0.70718 to 0.70820 (**Table**

315 **1**). The $^{143}Nd/^{144}Nd_{(i)}$ ratios of the porphyritic granite samples vary from 0.51234 to

316 0.51242 (ϵNd values of -3.85 to -5.38), and the $^{143}Nd/^{144}Nd_{(i)}$ ratios of monzonite and

317 monzodiorite samples vary from 0.51228 to 0.51245 (ϵNd values of -3.22 to -6.45).

318 A dioritic enclave sample has a $^{87}Sr/^{86}Sr_{(i)}$ ratio of 0.70718 and a $^{143}Nd/^{144}Nd_{(i)}$ ratio of

319 0.51244 (ϵNd value of -3.4). The evolved samples from the Pınarbaşı intrusion (Gt-

320 15 with 68.5 wt.% SiO_2 , and Gt-06 with 68.7 wt.% SiO_2) have higher $^{87}Sr/^{86}Sr_{(i)}$

321 ratios (0.70923 and 0.70855, respectively) even though there are no significant

322 differences in the $^{143}Nd/^{144}Nd_{(i)}$ ratios (Gt-06: 68.7 wt.% SiO_2 with 0.51236

323 $^{143}Nd/^{144}Nd_{(i)}$ ratio and Gt-09: 61.2 wt.% SiO_2 with 0.51245 $^{143}Nd/^{144}Nd_{(i)}$ ratio)

324 between the most and least evolved samples of the Pınarbaşı. **Figure 8a** shows the

325 initial Sr and Nd isotopic compositions of the samples, the potential source

326 reservoirs, Oligo–Miocene (OMG) and Eocene felsic intrusions (EOG), Simav
327 volcanic rocks (SMV), Baklan felsic intrusions (BG), and Kula volcanic rocks (KV). In
328 the Nd vs Sr isotope space (**Fig. 8a**), the Pınarbaşı intrusion samples fall along an
329 array indicating crustal contamination of mantle-derived melts. The correlation
330 between $^{143}\text{Nd}/^{144}\text{Nd}_{(i)}$ and $^{87}\text{Sr}/^{86}\text{Sr}_{(i)}$ ratios is slightly negative and all samples
331 overlap with the compositions of the Eastern Mediterranean Sea Sediments (EMMS),
332 OMG, and SMV (**Fig. 8a**). In contrast, they have higher $^{87}\text{Sr}/^{86}\text{Sr}_{(i)}$ and $^{143}\text{Nd}/^{144}\text{Nd}_{(i)}$
333 ratios than those of the BG samples.

334
335 The Pınarbaşı samples yield a relatively restricted range of $^{206}\text{Pb}/^{204}\text{Pb}_{(i)}$,
336 $^{207}\text{Pb}/^{204}\text{Pb}_{(i)}$, and $^{208}\text{Pb}/^{204}\text{Pb}_{(i)}$ ratios (**Figs. 8b-c**). The monzonite and monzodiorite
337 sample ranges are, respectively, 18.935–19.021, 15.716–15.724 and 39.070–39.091,
338 and the porphyritic granite sample ranges are 18.936–18.951, 15.717–15.721 and
339 39.068–39.082, respectively (**Table 2**). A dioritic enclave sample has the least
340 radiogenic $^{206}\text{Pb}/^{204}\text{Pb}_{(i)}$, $^{207}\text{Pb}/^{204}\text{Pb}_{(i)}$, and $^{208}\text{Pb}/^{204}\text{Pb}_{(i)}$ ratios of 18.939, 15.717, and
341 39.065, respectively. All samples plot above the Upper Crust curve (**Zartman and**
342 **Doe 1981**) and partly overlap with the compositions of the basement metamorphic
343 rocks, the Eğrigöz granitoid (EG), and the SMV (**Fig. 8b**). In contrast, they have more
344 radiogenic $^{206}\text{Pb}/^{204}\text{Pb}_{(i)}$, and $^{207}\text{Pb}/^{204}\text{Pb}_{(i)}$ ratios than the Kula volcanic rocks (KV).
345 On the $^{206}\text{Pb}/^{204}\text{Pb}_{(i)}$ vs $^{208}\text{Pb}/^{204}\text{Pb}_{(i)}$ diagram (**Fig. 8c**), they also intersect the EMSS
346 field comprising Sahara desert dust, Nile sediments, and minor Tethyan ophiolitic
347 and arc volcanic rocks from the Hellenic trench, which were traced in Stromboli
348 volcanic rocks along the Aeolian arc (**Klaver et al. 2015**), and have a less radiogenic
349 $^{208}\text{Pb}/^{204}\text{Pb}_{(i)}$ ratio compared to basement metamorphic rocks (**Fig. 8c**). In **Figure 8d**,
350 all samples from Pınarbaşı display $^{87}\text{Sr}/^{86}\text{Sr}_{(i)}$ trending towards the subducted

351 sediment-rich Enriched Mantle II end member (EM2; Zindler and Hart 1986), the
352 Global Subducted Sediments end member (GLOSS; Plank and Langmuir 1998), and
353 basement metamorphic rocks (MMM, higher radiogenic Sr reservoirs) with nearly
354 constant $^{206}\text{Pb}/^{204}\text{Pb}_{(i)}$ ratios.

355

356 *5.3. Molybdenite Re-Os geochronology*

357 The Re-Os age results for two molybdenite samples are presented in **Table 3** and
358 the analytical techniques are summarized in **Online Resource 1**. Two molybdenite
359 samples were selected from an outcrop (OKY-3-4) and a drill core (GOP-19m) from
360 the Pınarbaşı prospect. Sample OKY-3-4 was collected from a molybdenite–hematite
361 bearing silicified zone (**Fig. 4d**), and sample GOP-19m was taken from a 0.5-1cm
362 thick quartz–molybdenite–pyrite–chalcopyrite vein crosscutting a highly sericitized
363 porphyritic granite (**Fig. 4e**). The total Re concentrations of the molybdenite samples
364 are 950 and 1036 ppm and ^{187}Os concentrations are 181 and 199 ppb. Samples
365 OKY-3-4 and GOP-19m yield Re-Os ages of 18.3 ± 0.1 Ma and 18.2 ± 0.1 Ma,
366 respectively (Table 3).

367

368 **6. Discussion**

369 *6.1. Shallow-level magmatic processes*

370 Decreasing CaO, Fe_2O_3 , TiO_2 , P_2O_5 , and V trends with increasing SiO_2 are
371 consistent with pyroxene, apatite, and Fe–Ti oxide fractionation during the evolution
372 of the magmas of the Pınarbaşı intrusion (**see Online Resource 4**), and the
373 fractionated LREE element patterns and slightly negative Eu anomalies indicate
374 plagioclase fractionation during the evolution of the felsic pluton. In addition, the
375 negative correlation of Dy/Yb with SiO_2 (**Fig. 9a**), the positively correlated Zr/Sm ratio

376 and SiO₂ contents, as well as the slightly upward concave trend from MREEs to
377 HREEs (**Figs. 7b and 9b**) suggest low-pressure amphibole fractionation in the
378 presence of plagioclase. These fractionation trends, coupled with the negative
379 correlation of Al₂O₃, Na₂O, and Sr with SiO₂ are consistent with combined amphibole,
380 plagioclase, and pyroxene fractionation at low pressure, and the absence of high-
381 pressure garnet fractionation and garnet-bearing residue in the source (**see Online**
382 **Resource 4**; [Macpherson et al. 2006](#); [Davidson et al. 2007, 2013](#); [Alonso-Perez et](#)
383 [al. 2009](#); [Hora et al. 2009](#)).

384
385 The Pınarbaşı samples are characterized by upper continental crust-like
386 lithogeochemical compositions (**Figs. 7a-b**). On the ²⁰⁶Pb/²⁰⁴Pb_(i) vs ²⁰⁷Pb/²⁰⁶Pb_(i)
387 diagram (**Fig. 8b**), all Pınarbaşı samples plot above the Upper Crustal curve
388 ([Zartman and Doe 1981](#)) and overlap with the basement metamorphic rocks.
389 However, the Sr and Nd isotopic compositions together with A/CNK ratios of 3 to 2
390 and Mg# values of 30–47 for metamorphic basement ([Dilek et al. 2009](#)) are different
391 from those of the metamorphic basement rocks of the region. The high ⁸⁷Sr/⁸⁶Sr_(i)
392 ratios of the evolved samples of porphyritic granite (**Fig. 8a**; **Table 1**) are consistent
393 with upper crustal assimilation concomitant with fractional crystallization ([DePaolo](#)
394 [1981](#)). The 1/Sr vs. ⁸⁷Sr/⁸⁶Sr_(i) and SiO₂ vs. ²⁰⁸Pb/²⁰⁴Pb_(i) plots also show that the
395 porphyritic granite, which crosscuts the Pınarbaşı monzonite, reflects shallow-level
396 crustal assimilation during fractionation (**Figs. 9c-d**). On the ²⁰⁶Pb/²⁰⁴Pb_(i) vs
397 ⁸⁷Sr/⁸⁶Sr_(i) plot (**Fig. 8d**), the Pınarbaşı samples display a trend with variable ⁸⁷Sr/⁸⁶Sr_i
398 ratios for nearly constant ²⁰⁶Pb/²⁰⁴Pb_(i) ratios.

399

400

401 However, several compositional characteristics are attributed to source-inheritance
402 rather than to shallow-level crustal assimilation and fractionation only. They include
403 (1) the least radiogenic Sr compositions (**Fig. 8d**), (2) a low $^{208}\text{Pb}/^{204}\text{Pb}_{(i)}$ ratio distinct
404 with respect to the metamorphic basement (MMM in **Fig. 8c**), (3) samples with the
405 most radiogenic Nd isotopic compositions (**Fig. 8a**), and (4) enriched U and Pb
406 contents of the Pınarbaşı samples with respect to those of the metamorphic
407 basement (MMM in **Fig. 7a**). In summary, trace element patterns and Pb isotope
408 ratios indicate that the magmas at the origin of the Pınarbaşı intrusion have
409 assimilated middle to upper crustal materials.

410

411 *6.2 Source of magma*

412 In addition to fractional crystallization and assimilation (AFC) during evolution of the
413 Pınarbaşı magmas, there is geochemical and isotopic evidence for open-system
414 evolution, including partial melting, crust–mantle interaction, and enriched mantle
415 contributions. Partial melting of hydrous calc-alkaline to high-K calc-alkaline, and
416 basaltic to intermediate metamorphic rocks can produce moderate to mildly
417 peraluminous high-K, I-type granitoids (Rapp et al. 1991; Roberts and Clemens
418 1993; Rudnick and Gao 2003). This can explain the mildly peraluminous composition
419 of the Oligo–Miocene granitic rocks in western Anatolia (**Fig. 6d**), and they are
420 distinct with respect to the composition of metagraywacke and metapelite partial
421 melts (**Fig. 10a**).

422

423 The high-K and LILE-enriched (e.g., Ba, Sr) magmas can also be produced from the
424 influx of a LILE- and LREE-enriched- mantle melt at the base of the lower crust, and
425 this source could be produced by small to moderate degrees ($\leq 20\%$) of partial

426 melting of phlogopite–clinopyroxene–amphibole-bearing metasomatised lithospheric
427 mantle due to heating by asthenospheric upwelling (Lloyd et al. 1985; Foley 1992;
428 Conticelli et al. 2002; Grove et al. 2003; Condamine and Médard 2014). On the
429 La/Yb vs La diagram (Fig. 10b), the Pınarbaşı samples scatter between the partial
430 melting and fractional crystallization lines, suggesting partial melting of a lithospheric
431 mantle source contemporaneously with fractionation, and the highly variable Nb/Ta
432 ratio of the monzonitic and granitic samples between 7.9 and 34 (~11–12 for crust,
433 and ~17.5 for mantle; Green 1995) indicate fractional crystallization and low degrees
434 of partial melting. In addition, the high Rb/Sr (0.2–0.4) and highly variable Ba/Rb (7.5–
435 18.6) ratios of the Pınarbaşı samples are consistent with partial melting of a residual
436 hydrous phlogopite–amphibole- enriched mantle source (see Online Resource 2;
437 Furman and Graham 1999; Guo et al. 2013). The low Sm/Yb ratio below 3 of the
438 Pınarbaşı granitic and monzonitic samples (Fig. 10c) suggests a residue above the
439 garnet stability field at 35–40 km (Kay and Mpodozis 2001). The position of all
440 samples in the mantle–crust interaction field in the Nb–Y–Ga*3 ternary diagram of
441 Eby (1992) (Fig. 10d) is consistent with phlogopite–amphibole–pyroxene-bearing
442 lithospheric mantle–lower crust interactions.

443
444 Based on our geochemical data, the absence of residual garnet in the magma source
445 reflects a relatively thin crust in mid-western Anatolia since at least the Oligo–
446 Miocene. Geophysical data document a present-day average crustal thickness of 25
447 to 33 km in western Anatolia, and an average crustal thickness of 40 km during the
448 early Miocene (Dhont et al. 2006; Mutlu and Karabulut 2011; Karabulut et al. 2013).
449 Consequently, our results coupled with the crustal thickness of western Anatolia
450 allow us to conclude that enriched sub-continental lithospheric mantle interacted with

451 the lower crust and generated the parental magmas of the Oligo–Miocene granitic
452 intrusions at relatively low pressure (35–40 km).

453

454 6.3. Post-subduction tracers

455 Enrichment of LILEs (e.g., Ba, Rb, Sr), U and Pb, depletion of Nb and Ta, and high
456 Ba/La, Ba/Th, Rb/Y, Sr/Th and Sr/Nd ratios are attributed to fluid addition to the
457 mantle wedge from dehydration of a subducted slab (Pearce and Peate 1995;
458 Keppler 1996). By contrast, enrichment of Th, La, and Nb are attributed to
459 metasomatism of the mantle by melting of a subducted sedimentary component
460 (Tatsumi et al. 1986; Plank and Langmuir 1993; Brenan et al. 1995; Pearce and
461 Peate 1995; Plank 2005).

462

463 All samples of the Pınarbaşı intrusion, together with the Oligo-Miocene granitic rocks
464 of the western Aegean, exhibit variable Th/Yb ratios for nearly constant Ta/Yb ratios
465 (Fig. 11a), and reflect a subduction-related environment. The wide range of Ba (666–
466 2100 ppm), Sr (333–621 ppm) contents and high Ba/La (17.7–42.6) ratios of the
467 Pınarbaşı samples are consistent with addition of aqueous fluids derived from the
468 mantle wedge to the sub-lithospheric mantle. A narrow range of Nb/Y ratio with highly
469 variable Ba contents could also be attributed to slab-derived fluid enrichment (Fig.
470 11b). On the other hand, the relatively high Th/La (0.33–0.73), Th/Nb (1.0–2.3), Zr/Hf
471 (33.4–41.9, Zr/Hf = ~39.6 for EMSS) and a wide range of Th/Yb ratios (5.2–13.6;
472 excluding the high Th/Yb ratio of 31 of sample GOTK-18), as well as the low Ce/Pb
473 ratios (1.35–3.84; Ce/Pb = ~3.98 for EMSS and Ce/Pb = 2–3 for terrigenous
474 sediments; Lan et al. 1990; Klaver et al. 2015), with small negative Ce anomalies of
475 Pınarbaşı granitic and monzonitic rocks (Fig. 7a) could be indicative of a sedimentary

476 component mixed with an enriched mantle source. In the Nb/Y vs. Rb/Y plot (**Fig.**
477 **11c**), the Pınarbaşı samples exhibit a trend between melt-related enrichment and
478 slab-derived fluid enrichment array lines. These metasomatic agents are further
479 documented by the oblique trend between fluid- and melt-related enrichment trend
480 lines on the Th/Nb vs. Ba/Th plot (**Fig. 11d**) and also on the Ba/La vs Th/Yb plot (**Fig.**
481 **11e**). They have higher Ba/Nb and Th/Nb ratios than the EMSS and on the Th/Nb vs.
482 Ba/Nb diagram (**Fig. 11f**), they lie along both the sediment melting and aqueous fluid
483 trend lines. It is known that wet sediment melting can only occur at depths greater
484 than 100 km under relatively high temperatures (~800 °C) and the increased K, Th,
485 Ta, and Nb concentrations in arc-suites are attributed to the distance from the
486 subduction trenches, reflecting the heterogeneous mantle sources that change from
487 subduction-related to within-plate away from the trench and the low degree of partial
488 melting in the back-arc setting also leads to enrichment in incompatible elements
489 (Barragan et al. 1998; Aizawa et al. 1999; Duggen et al. 2007; Richards 2011; Müller
490 and Groves 2016). Therefore, the enrichment processes can be linked with
491 magmatism related to back-arc opening in the region as a consequence of hot
492 asthenospheric upwelling attributed either to slab rollback and subsequent slab tear
493 processes (Spakman et al. 1988; Jolivet and Brun 2010; van Hinsbergen 2010; Erkül
494 et al. 2013; Ersoy and Palmer 2013; Jolivet et al. 2013, 2015) or lithospheric
495 delamination and convective thinning of the lithospheric mantle (Dilek et al. 2009;
496 Altunkaynak et al. 2012a).

497

498 *6.4. Age of Mo-Cu Mineralization*

499 The early Miocene crystallization ages of molybdenite from the stockwork veins (18.3
500 ± 0.1 Ma and 18.2 ± 0.1 Ma) coincide with the crystallization and cooling ages of the

501 granitic rocks of the Oligo-Miocene magmatic pulse in western Anatolia (**Fig. 12**;
502 ~24.0 and 18 Ma; Isik et al. 2004; Ring and Collins 2005; Aydođan et al., 2008;
503 HasözbeK et al. 2010; Altunkaynak et al. 2012a). This indicates a very close
504 relationship of the mineralization event with the latest magmatic differentiation,
505 crystallization and subsequent cooling stages. In addition, the early Miocene age of
506 the Mo-Cu mineralization at Pınarbaşı shows that metal enrichment was closely
507 related to early Miocene post-orogenic magmatism (**Fig. 12**).

508
509

510 6.5. *Origin of metals in the porphyry-style Mo–Cu Pınarbaşı prospect*

511 The trace element data and the Sr, Nd, and Pb isotopic compositions of the
512 Pınarbaşı intrusive rocks suggest that the Mo–Cu-bearing monzonitic and granitic
513 rocks were derived from a melt that was produced by interaction of an enriched,
514 metasomatized lithospheric mantle and a lower crust at a depth of 35–40 km during
515 the Oligo–Miocene. The enriched melt influx from the metasomatized lithospheric
516 mantle into the lower crust resulted in partial melting of the lower crust at the
517 lithospheric mantle–lower crust interface. Lithospheric mantle interaction with the
518 lower crust likely increased through time, and lithospheric influx during the mid to late
519 Miocene probably resulted in thickening of the lower crust in western Anatolia (see
520 also discussion by Ersoy et al. 2010). This is consistent with the evolution of Oligo–
521 Miocene high-K calc-alkaline to middle Miocene shoshonitic magmatism in the region
522 interpreted as deep partial melting (Thorpe and Francis 1979). It is also in line with
523 the formation of an amphibole–garnet-bearing residual source during early to middle
524 Miocene magmatism (e.g., Ersoy et al. 2010; Çoban et al. 2012; Karaođlu and
525 Helvacı 2014).

Commented [A1]: The second part of this section discusses the origin of the metals. Therefore, it's probably best to keep this title as proposed by Okan.

526
527 Continuous partial melting of chalcophile and siderophile element-enriched lower
528 crustal amphibolitic cumulates and sub-continental lithospheric mantle can produce
529 H₂O-bearing, volatile-rich and fertile melts, which are the source of metals of
530 porphyry Au-Cu deposits in post-collisional extensional settings (Richards 2009; Hou
531 et al. 2011; Richards and Mumin 2013; Hou and Zhang 2014; Müller and Groves
532 2016). The crustal or mantle origin of the Mo-enrichment in porphyry systems is still
533 debated (Audétat 2010; Richards 2011). Pettke et al. (2010) advocated melting for
534 sub-continental metasomatised old mantle as the source of Mo for giant porphyry
535 Mo-rich systems in the Western U.S.A., and Mao et al (2011) suggested that
536 repeated melting of the lower crust can explain Mo-enrichment in back-arc
537 extensional settings during post-collisional magmatism. Molybdenum is enriched in
538 reduced sediments and is also immobile in low-temperature fluids (Crusius et al.
539 1996). Chondritic to super-chondritic ratios of Zr/Hf (33–42) and Hf/Sm (0.75–1.04) of
540 the Pınarbaşı intrusion reveal a terrigenous character of the subducted crustal
541 material (chondritic value of Hf/Sm: 0.75; Zr/Hf: 35–40, Patchett et al. 2004,
542 Claiborne et al. 2006). Therefore, our study reveals that melting of terrigenous
543 sediments can also supply Mo to an enriched lithospheric mantle source in a back-
544 arc setting. In light of these studies, it is concluded that a lithospheric mantle
545 metasomatised by fluids and subducted sediments, interacting at relatively low-
546 pressure conditions (depths of 35–40 km) with lower crust could explain the Mo–Cu
547 enrichment of the Pınarbaşı intrusion during back-arc magmatism (Fig. 12). The
548 over-thickened sub-continental lithospheric mantle during early to late Miocene could
549 have created the adequate environment for the evolution of larger scale Au ± Cu ±
550 Mo-rich deposits in western Anatolia (e.g., middle Miocene Uşak-Afyon-Konya

551 district, Kuşçu et al. 2011; Rabayrol et al 2014), because of continuous melting of
552 chalcophile and siderophile element-enriched amphibolite cumulates in the thickened
553 lower crust and the enriched lithospheric mantle.

554

555 *6.6. Tectonic setting, exhumation and epithermal overprint of the porphyry Mo–Cu*
556 *Pınarbaşı prospect*

557 Extensional tectonics favors the migration of highly oxidized, Cu-, Au- and Mo-rich
558 melts derived from the mantle and the lower crust into upper crustal levels
559 (Vigneresse 2007). The ore-bearing melt at the origin of the Pınarbaşı intrusion could
560 have rapidly ascended to mid-crustal levels with crustal assimilation along trans-
561 lithospheric faults activated during extension, and resulting in porphyry-style Mo-Cu
562 mineralization during the early Miocene (at ~18 Ma) that is consistent with the
563 differentiation-crystallization and cooling history of the Oligo-Miocene granites (24-18
564 Ma). The first, late Oligocene to early Miocene phase of extension in the region is
565 mainly characterized by the development of low-angle shear zones and the
566 subsequent emplacement and exhumation of granitic rocks along the ductile shear
567 zones (Fig. 12). Hence, the Oligo–Miocene felsic intrusions are regarded as syn-
568 extensional, that cooled rapidly along the footwall of detachment faults (Ring et al.
569 2003; Isik et al. 2004; Ring and Collins 2005; Dilek et al. 2009; Erkül 2010). The
570 second, middle to late Miocene extension phase in the region is characterized by the
571 development of high-angle normal faults forming graben structures in western
572 Anatolia (Yilmaz 1989; Hetzel et al. 1995; Ring et al. 2003; Fig. 12). The high-angle
573 normal faulting resulted in uplift of the graben shoulders, deep erosion and further
574 exhumation along the detachment footwalls, as well as cataclastic deformation of the
575 Oligo–Miocene granitic rocks (Yilmaz 1989; Dilek et al. 2009). Therefore, exhumation

576 of the Mo–Cu-bearing Pınarbaşı intrusion, exposed in the northwestern shoulder of
577 the Yenidoğmuş–YeniGediz graben, can be explained by uplift of the graben systems
578 (**Fig. 2, inset**). Further uplift during the middle to late Miocene may have resulted in
579 (1) removal of the shallow parts of the Pınarbaşı porphyry system in response to
580 rapid erosion, (2) telescoping by Sb±Ag±Au low-sulfidation epithermal mineralization,
581 and intense advanced argillic alteration at the Pınarbaşı prospect (**Figs. 5e-f; Oygür**
582 **and Erler 2000; Delibas et al. 2012a**). This is reminiscent of many porphyry systems
583 in post-collisional extensional settings (e.g., **Perello et al. 2001; Hou et al. 2009**).

584

585 **7. Conclusions**

586 The high-K calc-alkaline Pınarbaşı intrusion shares many geochemical features with
587 other calc-alkaline to high-K calc-alkaline Oligo–Miocene granitic rocks of western
588 Anatolia. The monzonitic and granitic rocks of Pınarbaşı were derived from
589 interactions of an enriched lithospheric mantle and lower crust at depth of 35–40 km
590 during Oligo–Miocene post-collisional magmatism. Trace-element ratios and distinct
591 Sr, Nd, and Pb isotopic compositions of the Pınarbaşı intrusion suggest that two
592 metasomatic agents could have been incorporated into the enriched mantle source
593 reflecting post-orogenic magmatism. We conclude that the lithospheric mantle was
594 metasomatized by fluids and subducted sediments, and its interaction with a lower
595 crust at low-pressure conditions explains the Mo and Cu enrichment of the Pınarbaşı
596 intrusion during back-arc magmatism. The ore-bearing melt of the Pınarbaşı intrusion
597 could have rapidly ascended to mid-crustal levels, with only limited crustal
598 assimilation along major trans-lithospheric faults as a result of the thinning of middle
599 to upper crust during regional extension, and resulted in the development of
600 porphyry-style mineralization during the early Miocene (~18 Ma). The subsequent

601 exhumation history of the Mo–Cu-bearing Pınarbaşı intrusion is attributed to regional-
602 scale uplift, and further exhumation along the detachment faults of the associated
603 core complexes during the middle to late Miocene. This evolution also resulted in an
604 overprint by epithermal mineralization, and intense advanced argillic alteration.

605

606 **Acknowledgments**

607 The authors would like to thank Fabio Capponi for XRF analyses (University of
608 Geneva) and Peter Laznicka (Metallogenica Consulting Adelaide), Cüneyt Baran,
609 Fatih Pekdemir, and Oktay Parlak (MTA) for help during fieldwork. Panagiotis
610 Voudouris and Albrecht von Quadt are thanked for their valuable comments and
611 suggestions that allowed us to improve the manuscript. We also thank associated
612 editor Frank Melcher for final edits. The research was supported by the “*Hacettepe*
613 *University Scientific Research Coordination Unit*” grants FHD-2015-7509 and FDS-
614 2015-7004, and the “*Swiss National Science Foundation*” through research grants
615 200020-155928. This research was also partially supported by the General
616 Directorate of Mineral Research and Exploration, Turkey (MTA)–*ETI Mine Works*
617 during the joint project 2002-32-57.d1. David Selby acknowledges the TOTAL
618 endowment fund. Seçil Delibaş and Burcu Kahraman (Hacettepe University) are
619 thanked for providing various pieces of information allowing us to finalize the
620 manuscript. This paper is dedicated to the memory of the senior author Okan
621 Delibaş, who dramatically passed away in August 2016 during the final revision
622 stages of the manuscript. Okan still had so many scientific projects in mind, his death
623 is a big loss to all of us, including his family, friends, colleagues and the international
624 scientific community.

625

626 **References**

- 627 Aghazadeh M, Hou Z, Badrzadeh Z, Zhou L (2015) Temporal–spatial distribution and
628 tectonic setting of porphyry copper deposits in Iran: Constraints from zircon U–Pb
629 and molybdenite Re–Os geochronology. *Ore Geol Rev* 70: 385-406
- 630 Agostini S, Doglioni C, Innocenti F, Manetti P, Tonarini S, Savaşçın M (2007) The
631 transition from subduction-related to intraplate Neogene magmatism in the Western
632 Anatolia and Aegean area. In Beccaluva L, Bianchini G, Wilson M (eds) *Cenozoic*
633 *Volcanism in the Mediterranean Area*. *Geol Soc Am Spec Paper* 418: 1–15
- 634 Agostini S, Doglioni C, Innocenti F, Manetti P, Tonarini S (2010) On the
635 geodynamics of the Aegean rift. *Tectonophysics* 488: 7–21
- 636 Aizawa Y, Tatsumi Y, Yamada H (1999) Element transport by dehydration of
637 subducted sediments: Implication for arc and ocean island magmatism. *Isl Arc* 8: 38–
638 46
- 639
- 640 Akdeniz N, Konak N (1979) Geology of the Simav-Emet-Tavşanlı-Dursunbey-Demirci
641 region. Report, General Directorate of Mineral Research and Exploration, Turkey
642 (MTA) Report No: 6547, Ankara (unpublished, in Turkish)
- 643
- 644 Aldanmaz E, Pearce JA, Thirlwall MF, Mitchell, JG (2000) Petrogenetic evolution of
645 late Cenozoic, post-collision volcanism in western Anatolia, Turkey. *J Volcanol Geoth*
646 *Res* 102: 67–95
- 647
- 648 Alici P, Temel A, Gourgaud A (2002) Pb-Nd-Sr isotope and trace element
649 geochemistry of Quaternary extension-related alkaline volcanism: A case study of

650 Kula region (western Anatolia, Turkey). *J Volcanol Geoth Res* 115: 487–510
651
652 Alonso-Perez R, Müntener O, Ulmer P (2009) Igneous garnet and amphibole
653 fractionation in the roots of island arcs: Experimental constraints on andesitic liquids.
654 *Contrib Mineral Petr* 157: 541–558
655
656 Altunkaynak Ş, Dilek Y (2006) Timing and nature of postcollisional volcanism in
657 western Anatolia and geodynamic implications. In Dilek Y, Pavlides, S (eds)
658 Postcollisional tectonics and magmatism in the Mediterranean region and Asia. *Geol*
659 *Soc Am Spec Paper* 409: 321–351
660
661 Altunkaynak Ş, Dilek Y, Genç CŞ, Sunal G, Gertisser R, Furnes H, Foland KA, Yang,
662 J (2012a) Spatial, temporal and geochemical evolution of Oligo-Miocene granitoid
663 magmatism in western Anatolia, Turkey. *Gondwana Res* 21: 961–986
664
665 Altunkaynak Ş, Sunal G, Aldanmaz E, Genç CŞ, Dilek Y, Furnes H, Foland, KA,
666 Yang J, Yildiz M (2012b) Eocene granitic magmatism in NW Anatolia (Turkey)
667 revisited: New implications from comparative zircon SHRIMP U-Pb and $^{40}\text{Ar}/^{39}\text{Ar}$
668 geochronology and isotope geochemistry on magma genesis and emplacement.
669 *Lithos* 155: 289–309
670
671 Arikas K, Voudouris P (1998) Hydrothermal alterations and mineralizations of
672 magmatic rocks in the southeastern Rhodope Massif. *Acta Vulcanologica* 10: 353-
673 365
674

675 Audetat A (2010) Source and evolution of molybdenum in the porphyry Mo(-Nb)
676 deposit at Cave Peak, Texas. *J Petrol* 51: 1739–1760
677

678 Aydoğan MS, Çoban H, Bozcu M, Akinci Ö (2008) Geochemical and mantle-like
679 isotopic (Nd, Sr) composition of the Baklan Granite from the Muratdağı Region
680 (Banaz, Uşak), western Turkey: Implications for input of juvenile magmas in the
681 source domains of western Anatolia Eocene-Miocene granites. *J Asian Earth Sci* 33:
682 155–176
683

684 Barragan R, Geist D, Hall M, Larson P, Kurz M (1998) Subduction controls on the
685 compositions of lavas from the Ecuadorian Andes. *Earth Planet Sci Lett* 154: 153-
686 166
687

688 Bozkurt E (2004) Granitoid rocks of the southern Menderes Massif (southwestern
689 Turkey): field evidence for Tertiary magmatism in an extensional shear zone. *Int J*
690 *Earth Sci* 93: 52–71
691

692 Bozkurt E, Park RG (1997) Evolution of a mid-Tertiary extensional shear zone in the
693 southern Menderes Massif, western Turkey. *Bull Soc Geol France* 168: 3–14
694

695 Bozkurt E, Sözbilir H (2004) Tectonic evolution of the Gediz Graben: field evidence
696 for an episodic, two-stage extension in western Turkey. *Geol Mag* 141: 63–79
697

698 Bozkurt E, Park RG, Winchester JA (1993) Evidence against the core/cover
699 interpretation of the southern sector of the Menderes Massif, west Turkey. *Terra*

700 Nova 5: 445–451

701

702 Brenan JM, Shaw HF, Ryerson FJ, Phinney DL (1995) Mineral-aqueous fluid
703 partitioning of trace elements at 900°C and 2.0 GPa: Constraints on the trace
704 element chemistry of mantle and deep crustal fluids. *Geochim Cosmochim Acta* 59:
705 3331–3350

706

707 Candan O, Çetinkaplan M, Oberhänsli R, Rimmelé G, Akal C (2005) Alpine high-
708 P/low-T metamorphism of the Afyon Zone and implications for the metamorphic
709 evolution of Western Anatolia, Turkey. *Lithos* 84: 102–124

710

711 Chiaradia M, Muntener O, Beate B (2011) Enriched basaltic andesites from mid-
712 crustal fractional crystallization, recharge, and assimilation (Pilavo Volcano, western
713 Cordillera of Ecuador). *J Petrol* 52: 1107–1141

714

715 Chakrabarti R, Basu, AR, Ghatak A (2012) Chemical geodynamics of Western
716 Anatolia. *Int Geol Rev* 54: 227–248

717

718 Claiborne L, Miller CF, Walker BA, Wooden JL, Mazdab FK, Bea F (2006) Tracking
719 magmatic processes through Zr/Hf ratios in rocks and Hf and Ti zoning in zircons: An
720 example from the Spirit Mountain batholith, Nevada. *Mineral Mag* 70: 517–543

721

722 Collins AS, Robertson AHF (1997) Lycian melange, southwestern Turkey: An
723 emplaced Late Cretaceous accretionary complex. *Geology* 25: 255–258

724

725 Condamine P, Médard E (2014) Experimental melting of phlogopite-bearing mantle
726 at 1 GPa: Implications for potassic magmatism. *Earth Planet Sci Lett* 397: 80–92
727

728 Conticelli S, Antonio MD, Pinarelli L, Civetta L, Federico N (2002) Source
729 contamination and mantle heterogeneity in the genesis of Italian potassic and
730 ultrapotassic volcanic rocks: Sr-Nd-Pb isotope data from Roman Province and
731 Southern Tuscany. *Mineral Petrol* 74: 189–222
732

733 Crusius J, Calvert S, Pedersen T, Sage D (1996) Rhenium and molybdenum
734 enrichments in sediments as indicators of oxic, suboxic and sulfidic conditions of
735 deposition. *Earth Planet Sci Lett* 145: 65–78
736

737 Çoban H, Karacik Z, Ece ÖI (2012) Source contamination and tectonomagmatic
738 signals of overlapping Early to Middle Miocene orogenic magmas associated with
739 shallow continental subduction and asthenospheric mantle flows in Western Anatolia:
740 A record from Simav (Kütahya) region. *Lithos* 140-141: 119–141
741

742 Davidson J, Turner S, Handley HK, Macpherson C, Dosseto A (2007) Amphibole
743 “sponge” in arc crust? *Geology* 35: 787–790
744

745 Davidson J, Turner S, Plank T (2013) Dy/Dy*: Variations arising from mantle sources
746 and petrogenetic processes. *J Petrol* 54: 525–537

747 Delaloye M, Bingöl E (2000) Granitoids from Western and Northwestern Anatolia:
748 Geochemistry and Modeling of Geodynamic Evolution. *Int Geol Rev* 42: 241–268
749

750 Delibaş O, Parlak O, Pekdemir F, Baran C (2012a) The Pınarbaşı granitoid (Gediz-
751 Kütahya) Mo-Cu, Pb-Zn and Sb±Ag mineralizations: an example of the polymetallic
752 mineralizations from the Mid-West Anatolia. *Yerbilimleri* 33: 151–176 (in Turkish)
753

754 Delibaş O, Baran C, Pekdemir F (2012b) Pınarbaşı (Kütahya-GedizGediz) region
755 2010-2011 mineral exploration and ore geology report. General Directorate of
756 Mineral Research and Exploration, Turkey (MTA). Report No: 6580, Ankara
757 (unpublished, in Turkish)
758

759 DePaolo DJ (1981) Trace element and isotopic effects of combined wallrock
760 assimilation and fractional crystallization. *Earth Planet Sci Lett* 53: 189–202
761

762 Dhont D, Chorowicz J, Luxey P (2006) Anatolian escape tectonics driven by Eocene
763 crustal thickening and Neogene–Quaternary extensional collapse in the eastern
764 Mediterranean region. In Dilek Y, Pavlides, S (eds) *Postcollisional tectonics and*
765 *magmatism in the Mediterranean region and Asia*. *Geol Soc Am Spec Paper* 409:
766 441–462
767

768 Dilek Y (2006) Collision tectonics of the Mediterranean region: causes and
769 consequences. In: Dilek Y, Pavlides S (eds) *Postcollisional tectonics and magmatism*
770 *in the Mediterranean Region and Asia*. *Geol Soc Am Spec Paper* 409: 1-13
771

772 Dilek Y, Sandvol E (2009) Seismic structure, crustal architecture and tectonic
773 evolution of the Anatolian-African plate boundary and the Cenozoic orogenic belts in
774 the Eastern Mediterranean region. In Murphy JB, Keppie JD, Hynes AJ (eds) *Ancient*

775 orogens and modern analogues. *Geol Soc London Spec Pub* 327: 127–160
776
777 Dilek Y, Altunkaynak Ş (2010) Geochemistry of Neogene–Quaternary alkaline
778 volcanism in western Anatolia, Turkey and implications for the Aegean mantle. *Int*
779 *Geol Rev* 52: 631–655
780
781 Dilek Y, Altunkaynak Ş, Oner Z (2009) Syn-extensional granitoids in the Menderes
782 core complex and the late Cenozoic extensional tectonics of the Aegean province. In
783 Ring U, Wernicke B (eds) *Extending a continent: Architecture, rheology and heat*
784 *budget*. *Geol Soc London Spec Pub* 321: 197–223
785
786 Doglioni C, Agostini S, Crespi M, Innocenti F, Manetti P, Riguzzi F, Savaşçın MY
787 (2002) On the extension in western Anatolia and the Aegean sea. In Rosenbaum G,
788 Lister GS (eds) *India-Asia convergence in NW Himalaya: Reconstruction of the*
789 *evolution of the Alpine-Himalayan Orogen*. *J Virtual Explor* 7: 167–181
790
791 Duggen S, Portnyagin M, Baker J, Ulfbeck D, Hoernle K, Garbe-Schönberg D,
792 Grassineau N (2007) Drastic shift in lava geochemistry in the volcanic-front to rear-
793 arc region of the Southern Kamchatkan subduction zone: Evidence for the transition
794 from slab surface dehydration to sediment melting. *Geochim Cosmochim Acta* 71:
795 452–480
796
797 Eby GN (1992) Chemical subdivision of the A-type granitoids: Petrogenetic and
798 tectonic implications. *Geology* 20: 641–644
799

800 Erkül F (2010) Tectonic significance of synextensional ductile shear zones within the
801 Early Miocene Alaçamdağ granites, northwestern Turkey. *Geol Mag* 147: 611–637
802

803 Erkül ST, Erkül F (2012) Magma interaction processes in syn-extensional granitoids:
804 The Tertiary Menderes metamorphic core complex, western Turkey. *Lithos* 142-143:
805 16–33
806

807 Erkül F, Erkül ST, Ersoy Y, Uysal I, Klötzli, U (2013) Petrology, mineral chemistry and
808 Sr-Nd-Pb isotopic compositions of granitoids in the central Menderes metamorphic
809 core complex: Constraints on the evolution of Aegean lithosphere slab. *Lithos* 180-
810 181: 74–91
811

812 Ersoy EY, Palmer MR (2013) Eocene–Quaternary magmatic activity in the Aegean:
813 Implications for mantle metasomatism and magma genesis in an evolving orogeny.
814 *Lithos* 180-181: 5-24
815

816 Ersoy EY, Helvacı C, Palmer MR (2010) Mantle source characteristics and melting
817 models for the early-middle Miocene mafic volcanism in Western Anatolia:
818 Implications for enrichment processes of mantle lithosphere and origin of K-rich
819 volcanism in post-collisional settings. *J Volcanol Geoth Res* 198: 112–128
820

821 Foley S (1992) Potassic and ultrapotassic magmas and their origin vein-plus-wall-
822 rock melting mechanisms in the lithosphere and the origin of potassic alkaline
823 magmas. *Lithos* 28: 435–453
824

825 Furman T, Graham D (1999) Erosion of lithospheric mantle beneath the East African
826 Rift system: geochemical evidence from the Kivu volcanic province. *Lithos* 48: 237–
827 262
828
829 Fytikas M, Innocenti F, Manetti P, Peccerillo A, Mazzuoli R, Villari L (1984) Tertiary to
830 Quaternary evolution of volcanism in the Aegean region. In Dixon JE, Robertson AHF
831 (eds), *The geological evolution of the Eastern Mediterranean* Geol Soc London Spec
832 Pub 17: 687–699
833
834 Green TH (1995) Significance of Nb/Ta as an indicator of geochemical processes in
835 the crust-mantle system. *Chem Geol* 120: 347–359
836
837 Grove TL, Elkins-Tanton L, Parman SW, Chatterjee N, Müntener O, Gaetani GA
838 (2003) Fractional crystallization and mantle-melting controls on calc-alkaline
839 differentiation trends. *Contrib Mineral Petr* 145: 515–533
840
841 Gökçe A, Spiro B (1994) Stable isotope study of antimony deposits in the Muratdağı
842 Region, Western Turkey. *Miner Deposita* 29: 361-365
843
844 Guo Z, Wilson M, Zhang M, Cheng Z, Zhang L (2013) Post-collisional, K-rich mafic
845 magmatism in south Tibet: Constraints on Indian slab-to-wedge transport processes
846 and plateau uplift. *Contrib Mineral Petr* 165: 1311–1340
847
848 Güleç N (1991) Crust–mantle interaction in western Turkey: implications from Sr and
849 Nd isotope geochemistry of Tertiary and Quaternary volcanics. *Geol Mag* 128: 417–

850 435
851
852 Gürboğa Ş, Koçyiğit A, Ruffet G, Koçyiğit A, Ruffet G (2013) Episodic two-stage
853 extensional evolutionary model for southwestern Anatolian graben-horst system:
854 New field data from the Erdoğmuş-Yenigediz graben (Kütahya). *J Geodyn* 65: 176–
855 198
856
857 Harris NB, Kelley S, Okay A (1994) Post-collision magmatism and tectonics in
858 northwest Anatolia. *Contrib Mineral Petr* 117: 241–252
859
860 Hasözbeğ A, Akay E, Erdoğan B, Satir M, Siebel W (2010) Early Miocene granite
861 formation by detachment tectonics or not? A case study from the northern Menderes
862 Massif (Western Turkey). *J Geodyn* 50: 67–80
863
864 Helvacı C, Ersoy Y, Sözbilir H, Erkül F, Sümer Ö, Uzel B (2009) Geochemistry and
865 $^{40}\text{Ar}/^{39}\text{Ar}$ geochronology of Miocene volcanic rocks from the Karaburun Peninsula:
866 implications for amphibole-bearing lithospheric mantle source, Western Anatolia. *J*
867 *Volcanol Geoth Res* 185: 181–202
868
869 Hetzel R, Ring U, Akal C., Troesch M (1995) Miocene NNE-directed extensional
870 unroofing in the Menderes Massif, southwestern Turkey. *J Geol Soc London* 152:
871 639–654
872
873 Hofmann AW (1997) Mantle geochemistry: the message from oceanic volcanism.
874 *Nature* 385: 219–229

875
876 Hora JM, Singer BS, Wörner G, Beard BL, Jicha BR, Johnson CM (2009) Shallow
877 and deep crustal control on differentiation of calc-alkaline and tholeiitic magma. *Earth*
878 *Planet Sci Lett* 285: 75–86
879
880 Hou Z, Zhang H (2014) Geodynamics and metallogeny of the eastern Tethyan
881 metallogenic domain. *Ore Geol Rev* 70: 346-384
882
883 Hou Z, Yang Z, Qu X, Meng X, Li Z, Beaudoin G, Rui Z, Gao Y, Zaw K (2009) The
884 Miocene Gangdese porphyry copper belt generated during post-collisional extension
885 in the Tibetan Orogen. *Ore Geol Rev* 36: 25–51
886
887 Hou Z, Zhang H, Pan X, Yang Z (2011) Porphyry Cu(-Mo-Au) deposits related to
888 melting of thickened mafic lower crust: Examples from the eastern Tethyan
889 metallogenic domain. *Ore Geol Rev* 39: 21–45
890
891 Innocenti F, Agostini S, Di Vincenzo G, Doglioni C, Manetti P, Savaşçın MY, Tonarini
892 S (2005) Neogene and Quaternary volcanism in Western Anatolia: magma sources
893 and geodynamic evolution. *Mar Geol* 221: 97–421
894
895 Isik V, Tekeli O, Seyitoglu G (2004) The $^{40}\text{Ar}/^{39}\text{Ar}$ age of extensional ductile
896 deformation and granitoid intrusion in the northern Menderes core complex:
897 Implications for the initiation of extensional tectonics in western Turkey. *J Asian Earth*
898 *Sci* 23: 555–566
899

900 Jackson SE (2008) Lamtrace data reduction software for LA-ICP-MS. In Sylvester P
901 (ed) Laser Ablation ICP-MS in the Earth sciences: Current practices and outstanding
902 issues. Mineral Ass Canada Short Course 40: 305–307
903

904 Jacobsen SB, Wasserburg GJ (1984) Sm–Nd isotopic evolution of chondrites and
905 achondrites. *Earth Planet Sci Lett* 67: 137–150
906

907 Jolivet L, Brun JP (2010) Cenozoic geodynamic evolution of the Aegean. *Int J Earth
908 Sci* 99: 109–138
909

910 Jolivet L, Faccenna C, Goffe B, Burov E, Agard P (2003) Subduction tectonics and
911 exhumation of high-pressure metamorphic rocks in the Mediterranean orogens. *Am J
912 Sci* 303: 353–409
913

914 Jolivet L, Faccenna C, Huet B, Labrousse L, Le Pourhiet L, Lacombe O, Lecomte E,
915 Burov E, Denèle Y, Brun JP, Philippon M, Paul A, Salaün G, Karabulut H, Piromallo
916 C, Monié P, Gueydan F, Okay A, Oberhänsli R, Pourteau A, Augier R, Gadenne L,
917 Driussi O (2013) Aegean tectonics: Strain localisation, slab tearing and trench
918 retreat. *Tectonophysics* 597-598: 1–33
919

920 Jolivet L, Menant A, Sternai P, Rabillard A, Arbaret L, Augier R, Laurent V, Beaudoin
921 A, Grasemann B, Huet B, Labrousse L, Le L (2015) The geological signature of a
922 slab tear below the Aegean. *Tectonophysics* 659: 166–182
923
924

925 Kaiser-Rohrmeier M, von Quadt A, Driesner T, Heinrich CA, Handler R, Ovtcharova
926 M, Ivanov Z, Petrov P, Sarov S, Peytcheva I (2013) Post-orogenic extension and
927 hydrothermal ore formation: High-precision geochronology of the central Rhodopian
928 metamorphic core complex (Bulgaria-Greece). *Econ Geol* 108: 691–718
929

930 Karabulut H, Paul A, Afacan ET, Hatzfeld D, Childs DM, Aktar M (2013) Long-
931 wavelength undulations of the seismic Moho beneath the strongly stretched Western
932 Anatolia. *Geophys J Int* 194: 450–464
933

934 Karaoğlu Ö, Helvacı C (2014) Isotopic evidence for a transition from subduction to
935 slab-tear related volcanism in western Anatolia, Turkey. *Lithos* 192-195: 226–239
936

937 Karaoğlu Ö, Helvacı C, Ersoy EY (2010) Petrogenesis and $^{40}\text{Ar}/^{39}\text{Ar}$ geochronology
938 of the volcanic rocks of the Uşak–Güre basin, western Turkey. *Lithos* 119: 193–210
939

940 Kay S, Mpodozis C (2001) Cenrtal Andean ore deposits linked to evolving shallow
941 subduction systems and thickening crust. *Geol Soc Am Today* 11: 4-9
942

943 Keppler H (1996) Constraints from partitioning experiments on the composition of
944 subduction-zone fluids. *Nature* 380: 237-240
945

946 Klaver M, Djuly T, de Graaf S, Sakes A, Wijbrans J, Davies G, Vroon P (2015)
947 Temporal and spatial variations in provenance of Eastern Mediterranean Sea
948 sediments: Implications for Aegean and Aeolian arc volcanism. *Geochim Cosmochim*
949 *Acta* 153: 149–168

950

951 Koçyiğit A, Unay E, Sarac G (2000) Episodic graben formation and extensional
952 neotectonic regime in west-central Anatolia and the Isparta angle: A case study in the
953 Akşehir-Afyon graben, Turkey. In Bozkurt E, Winchester JA, Piper JDA (eds)
954 Tectonics and magmatism in Turkey and surrounding area, Geol Soc London Spec
955 Pub 173: 405–421

956

957 Koprubasi N, Aldanmaz E (2004) Geochemical constraints on the petrogenesis of
958 Cenozoic I-type granitoids in northwest Anatolia, Turkey: Evidence for magma
959 generation by lithospheric delamination in a post-collisional setting. *Int Geol Rev* 46:
960 705–729

961

962 Kroll T, Muller D, Seifert T, Herzig PM, Schneider A (2002) Petrology and
963 geochemistry of the shoshonite-hosted Skouries porphyry Cu-Au deposit, Chalkidiki,
964 Greece. *Miner Deposita* 37: 137–144

965

966 Kuşçu İ, Gençaliolu-Kuşçu G, Tosdal R, Ulrich T, Freidman R (2011) The
967 geochronology of gold-copper deposition and temporal association with magmatic
968 rocks in western Anatolia. 64th Geological Congress of Turkey, Ankara, April 25-29,
969 2011. Abstracts book: 189-190

970

971 Lan CY, Lee T, Wang Lee C (1990) The Rb-Sr isotopic record in Taiwan gneisses
972 and its tectonic implication. *Tectonophysics* 183: 129-143

973

974

975 Lloyd FE, Arima M, Edgar AD (1985) Partial melting of a phlogopite-clinopyroxenite
976 nodule from south-west Uganda: an experimental study bearing on the origin of
977 highly potassic continental rift volcanics. *Contrib Mineral Petr* 91: 321–329
978

979 Macpherson CG, Dreher ST, Thirlwall MF (2006) Adakites without slab melting: High
980 pressure differentiation of island arc magma, Mindanao, the Philippines. *Earth Planet
981 Sci Lett* 243: 581–593
982

983 Mao JW, Pirajno F, Xiang JF, Gao JJ, Ye HS, Li YF, Guo BJ (2011) Mesozoic
984 molybdenum deposits in the east Qinling-Dabie orogenic belt: Characteristics and
985 tectonic settings. *Ore Geol Rev* 43: 264–293
986

987 Marchev P, Kaiser-Rohrmeier B, Heinrich C, Ovtcharova M, von Quadt A, Raicheva
988 R (2005) Hydrothermal ore deposits related to post-orogenic extensional magmatism
989 and core complex formation: The Rhodope Massif of Bulgaria and Greece. *Ore Geol
990 Rev* 27: 53-89
991

992 Márton I, Moritz R, Spikings R (2010) Application of low-temperature
993 thermochronology to hydrothermal ore deposits: formation, preservation and
994 exhumation of epithermal gold system from the Eastern Rhodopes, Bulgaria.
995 *Tectonophysics* 483: 240–254
996

997 Middlemost EAK (1994) Naming materials in the magma/igneous rock system.
998 *Earth- Sci Rev* 37: 215–224

999

1000 Moritz R, Márton I, Orтели M, Marchev P, Voudouris P, Bonev N, Spikings R, Cosca
1001 M (2010) A review of age constraints of epithermal precious and base metal deposits
1002 of the Tertiary Eastern Rhodopes: coincidence with Late Eocene–Early Oligocene
1003 tectonic plate reorganization along the Tethys. In Christofides G, Kantiradis N,
1004 Kostopoulos DS, Chatziperos AA (eds) Proceedings of the XIX Congress of the
1005 Carpathian Balkan Geological Association. Scientific Annals of the School of
1006 Geology, Thessaloniki, Greece: 351–358

1007

1008 Moritz R, Noverraz C, Marton I, Marchev P, Spikings RA, Fontignie DA,
1009 Spangenberg JE, Vennemann T, Kolev K, Hasson S (2014) Sedimentary-rock-
1010 hosted epithermal systems of the Tertiary Eastern Rhodopes, Bulgaria: new
1011 constraints from the Stremtsi gold prospect. In Garofalo PS, Ridley JS (eds) Gold-
1012 transporting hydrothermal fluids in the Earth's crust, Geol Soc London Spec Pub 402:
1013 207-230

1014

1015 Moritz R, Rezeau H, Ovtcharova M, Tayan R, Melkonyan R, Hovakimyan S,
1016 Ramazanov V, Selby D, Ulianov A, Chiaradia M, Putlitz B (2016) Long-lived,
1017 stationary magmatism and pulsed porphyry systems during Tethyan subduction to
1018 post-collision evolution in the southernmost Lesser Caucasus, Armenia and
1019 Nakhitchevan. *Gondwana Res* 37: 465-503

1020

1021 Müller D, Groves DI (2016) Potassic igneous rocks and associated gold-copper
1022 mineralization. Springer 4th ed, 311 p

1023

1024 Mutlu AK, Karabulut H (2011) Anisotropic Pn tomography of Turkey and adjacent
1025 regions. *Geophys J Int* 187: 1743–1758
1026

1027 Mutlu H, Sariz K, Kadir S (2005) Geochemistry and origin of the Şaphane alunite
1028 deposit, Western Anatolia, Turkey. *Ore Geol Rev* 26: 39–50
1029

1030 Okay A (2008) Geology of Turkey : A synopsis. *Anschnitt* 21: 19–42
1031

1032 Okay A, Tüysüz O (1999) Tethyan sutures of northern Turkey. In Durand B, Jolivet L,
1033 Horvath F, Seranne M (eds) *The Mediterranean basin: Tertiary extension within the*
1034 *Alpine orogen*. *Geol Soc London Spec Pub* 156: 475–515
1035

1036 Okay A, Satir M, Maluski H, Siyako M, Monie P, Metzger R, Akyüz S (1996) Paleo-
1037 and Neo-Tethyan events in northwestern Turkey: Geologic and geochronologic
1038 constraints. In Yin A, Harrison TM (eds) *The tectonic evolution of Asia*. Cambridge
1039 University press: 420–441
1040

1041 Okay A, Harris NBW, Kelley SP (1998) Exhumation of blueschists along a Tethyan
1042 suture in northwest Turkey. *Tectonophysics* 285: 275–299
1043

1044 Oygür V (1997) Anatomy of an epithermal mineralization: Mumcu (Balıkesir-Sındırgı),
1045 inner-western Anatolia, Turkey. *Miner Res Expl Bull* 119: 29–39
1046

1047 Oygür V, Eler A (2000) Metallogeny of Simav graben (Inner-Western Anatolia,
1048 Turkey). *Geol Bull Turkey* 43: 7–19

1049

1050 Oyman T, Özgenç I, Tokcaer M, Akbulut M (2013) Petrology, geochemistry, and
1051 evolution of the iron skarns along the northern contact of the Eğrigöz plutonic
1052 complex, western Anatolia, Turkey. *Turk J Earth Sci* 22: 61–97

1053

1054 Öner Z, Dilek Y (2011) Supradetachment basin evolution during continental
1055 extension: The Aegean province of western Anatolia, Turkey. *Geol Soc Am Bull* 123:
1056 2115-2141

1057

1058 Patchett PJ, Vervoort JD, Söderlund U, Salters VJM (2004) Lu-Hf and Sm-Nd
1059 isotopic systematics in chondrites and their constraints on the Lu-Hf properties of the
1060 Earth. *Earth Planet Sci Lett* 222: 29–41

1061

1062 Patiño Douce AE (1999) What do experiments tell us about the relative contributions
1063 of crust and mantle to the origin of granitic magmas? In Castro A, Fernandez C,
1064 Vigneresse JL (eds), *Understanding granites: Integrating new and classical*
1065 *techniques*. *Geol Soc London Spec Pub* 168: 55–75

1066

1067 Pe-Piper G, Piper DJW (2001) Late Cenozoic, post-collisional Aegean igneous rocks:
1068 Nd, Pb and Sr isotopic constraints on petrogenetic and tectonic models. *Geol Mag*
1069 138: 653–668

1070

1071 Pe-Piper G, Piper DJW (2007) Neogene backarc volcanism of the Aegean: New
1072 insights into the relationship between magmatism and tectonics. In Beccaluva L,
1073 Bianchini G, Wilson M (eds) *Cenozoic volcanism of the Aegean: New insights into the*

1074 relationship between magmatism and tectonics. Geol Soc Am Spec Paper 418: 17–
1075 31
1076
1077 Pearce JA (1983) Role of the sub-continental lithosphere in magma genesis at active
1078 continental margins. In Hawkesworth CJ, Norry MJ (eds) Continental basalts and
1079 mantle xenoliths. Shiva Publishing LTd, Cambridge, Mass: 230-249
1080
1081 Pearce JA, Peate DW (1995) Tectonic implications of the composition of volcanic arc
1082 magmas. Annu Rev Earth Planet Sc 23: 251–285
1083
1084 Peccerillo A, Taylor SR (1976) Geochemistry of Eocene calc-alkaline volcanic rocks
1085 from the Kastamonu area, northern Turkey. Contrib Mineral Petr 58: 63–81
1086
1087 Perello J, Cox D, Garamjav D, Sanjdorj S, Diakov S, Schissel D, Munkhbat TO, Oyun
1088 G (2001) Oyu Tolgoi, Mongolia: Siluro-Devonian porphyry Cu-Au(Mo) and high-
1089 sulfidation Cu Mineralization with a Cretaceous chalcocite blanket. Econ Geol 96:
1090 1407–1428
1091
1092 Pettke T, Oberli F, Heinrich CA (2010) The magma and metal source of giant
1093 porphyry-type ore deposits, based on lead isotope microanalysis of individual fluid
1094 inclusions. Earth Planet Sci Lett 296: 267–277
1095
1096 Plank T (2005) Constraints from Thorium/Lanthanum on sediment recycling at
1097 subduction zones and the evolution of the continents. J Petrol 46: 921–944
1098

1099 Plank T, Langmuir C (1993) Tracing trace elements from sediment input to volcanic
1100 output at subduction zones. *Nature* 362: 739–742
1101

1102 Plank T, Langmuir C (1998) The chemical composition of subducting sediment and
1103 its consequences for the crust and mantle. *Chem Geol* 145: 325–394
1104

1105 Pourteau A, Candan O, Oberhänsli R (2010) High-pressure metasediments in central
1106 Turkey: Constraints on the Neotethyan closure history. *Tectonics* 29: TC5004
1107

1108 Rabayrol F, Miskovic A, Hart CJR, Kuşçu İ, Sanchez M (2014) The Cenozoic
1109 metallogeny of Western Anatolia, Turkey. SEG 2014 Meeting: Building Exploration
1110 Capability for the 21st Century, Keystone, Colorado, USA, September 27-30 2016.
1111 [http://www.segweb.org/SEG/_Events/Conference_Website_Archives/2014/Conferen](http://www.segweb.org/SEG/_Events/Conference_Website_Archives/2014/Conference_Proceedings/data/index.htm)
1112 [ce_Proceedings/data/index.htm](http://www.segweb.org/SEG/_Events/Conference_Website_Archives/2014/Conference_Proceedings/data/index.htm), poster 0393-000197
1113

1114 Rapp RP, Watson, EB, Miller, CF (1991) Partial melting of amphibolite/eclogite and
1115 the origin of Archean trondhjemites and tonalites. *Precambrian Res* 51: 1–25
1116

1117 Rezeau H, Moritz R, Wotzlaw JF, Tayan R, Melkonyan R, Ulianov A, Selby D,
1118 d'Abzaz FX, Stern R (2016) Temporal and genetic link between incremental pluton
1119 assembly and pulsed porphyry Cu-Mo formation in accretionary orogens. *Geology*
1120 44: 627-630
1121

1122 Ribeiro JM, Stern RJ, Kelley KA, Martinez F, Ishizuka O, Manton WI, Ohara Y (2013)
1123 Nature and distribution of slab-derived fluids and mantle sources beneath the

1124 southeast Mariana forearc rift. *Geochem Geoph Geos* 14: 4585–4607
1125
1126 Richards JP (2009) Postsubduction porphyry Cu-Au and epithermal Au deposits:
1127 Products of remelting of subduction-modified lithosphere. *Geology* 37: 247–250
1128
1129 Richards JP (2011) Magmatic to hydrothermal metal fluxes in convergent and
1130 collided margins. *Ore Geol Rev* 40: 1–26
1131
1132 Richards JP, Mumin AH (2013) Magmatic-hydrothermal processes within an
1133 evolving Earth: Iron oxide-copper-gold and porphyry Cu±Mo±Au deposits. *Geology*
1134 41: 767–770
1135
1136 Ring U, Collins AS (2005) U-Pb SIMS dating of synkinematic granites: timing of core-
1137 complex formation in the northern Anatolide belt of western Turkey. *J Geol Soc*
1138 London 162: 289–298
1139
1140 Ring U, Gessner K, Güngör T, Passchier CW (1999) The Menderes massif of
1141 western Turkey and the Cycladic massif in the Aegean—do they really correlate? *J*
1142 *Geol Soc London* 156: 3–6
1143
1144 Ring U, Johnson C, Hetzel R, Gessner K (2003) Tectonic denudation of a Late
1145 Cretaceous-Tertiary collisional belt: regionally symmetric cooling patterns and their
1146 relation to extensional faults in the Anatolide belt of western Turkey. *Geol Mag* 140:
1147 421–441
1148

1149 Ring U, Glodny J, Will T, Thomson S (2010) The Hellenic subduction system: High-
1150 pressure metamorphism, exhumation, normal faulting, and large-scale extension.
1151 *Annu Rev Earth Planet Sc* 38: 45–76
1152

1153 Roberts MP, Clemens JD (1993) Origin of high-potassium, calc-alkaline, I-type
1154 granitoids. *Geology* 21: 825–828
1155

1156 Rudnick RL, Gao S (2003) Composition of the continental crust. In Rudnick RL,
1157 Holland HD, Turekian KK (eds), *The crust, Treatise on Geochemistry*, Elsevier: 1–64
1158

1159 Sánchez MG, McClay KR, King AR, Wijbrams JR (2016) Cenozoic crustal extension
1160 and its relationship to porphyry Cu-Au-(Mo) and epithermal Au-(Ag) mineralization in
1161 the Biga Peninsula, northwestern Turkey. In: Richards JP (ed), *Tectonics and
1162 metallogeny of the Tethyan orogenic belt, Soc Econ Geol Spec Pub* 19: 113–156
1163

1164 Selby D, Creaser RA (2001) Late and mid-Cretaceous mineralization in the northern
1165 Canadian Cordillera: Constraints from Re-Os molybdenite dates. *Econ Geol* 96:
1166 1461–1467
1167

1168 Seyitoglu G (1997) The Simav Graben: An example of young E-W trending structures
1169 in the Late Cenozoic extensional system of W. Turkey. *Turk J Earth Sci* 6: 135–141
1170

1171 Seyitoglu G, Scott BC, Rundle CC (1992) Timing of Cenozoic extensional tectonics in
1172 west Turkey. *J Geol Soc London* 149: 533–538
1173

1174 Sherlock SC (1999) Oscillatory zoned chrome lawsonite in the Tavşanlı zone,
1175 northwest Turkey. *Mineral Mag* 63: 687–692
1176

1177 Sillitoe RH (2002) Some metallogenic features of gold and copper deposits related to
1178 alkaline rocks and consequences for exploration. *Mineral Deposita* 37: 4–13
1179

1180 Smoliar MI, Walker RJ, Morgan JW (1996) Re-Os ages of group IIA, IIIA, IVA, and
1181 IVB iron meteorites. *Science* 271: 1099–1102

1182 Spakman W, Wortel MJR, Vlaar NJ (1988) The Hellenic subduction zone: A
1183 tomographic image and its geodynamic implications. *Geophys Res Lett* 15: 60–63
1184

1185 Sun SS, McDonough WF (1989) Chemical and isotopic systematics of oceanic
1186 basalts: implications for mantle composition and processes. In Saunders AD, Norry
1187 MJ (eds) *Magmatism in the ocean basins*. *Geol Soc London Spec Pub* 42: 313–345
1188

1189 Şengör AMC, Yılmaz Y (1981) Tethyan evolution of Turkey: A plate tectonic
1190 approach. *Tectonophysics* 75: 181–241
1191

1192 Şengör AMC, Satir M, Akkök R (1984) Timing of tectonic events in the Menderes
1193 massif, western Turkey: Implications for tectonic evolution and evidence for pan-
1194 African basement in Turkey. *Tectonics* 3: 693–707
1195

1196 Tatsumi Y, Hamilton DL, Nesbitt RW (1986) Chemical characteristics of fluid phase
1197 released from a subducted lithosphere and origin of arc magmas: Evidence from
1198 high-pressure experiments and natural rocks. *J Volcanol Geoth Res* 29: 293–309

1199

1200 Thirwall M, Smith TE, Graham AM, Theodorou N, Hollings P. Davidson JP, Arculus
1201 RD (1994) High field strength element anomalies in arc lavas: source or processes. *J*
1202 *Petrol* 35: 819–838

1203

1204 Thorpe RS, Francis PW (1979) Variations in Andean andesite compositions and their
1205 petrogenetic significance. *Tectonophysics* 57: 53–70

1206

1207 Tokay M, Doyuran V (1979) Seismotectonic features of Gediz and its surroundings.
1208 *Geol Bull Turkey* 22: 209–210 (in Turkish with English abstract)

1209

1210 van Hinsbergen DJJ (2010) A key extensional metamorphic complex reviewed and
1211 restored: The Menderes massif of western Turkey. *Earth-Sci Rev* 102: 60–76

1212

1213 van Hinsbergen DJJ, Schmid SM (2012) Map view restoration of Aegean–West
1214 Anatolian accretion and extension since the Eocene. *Tectonics* 31: TC5005

1215

1216 Vigneresse JL (2007) The role of discontinuous magma inputs in felsic magma and
1217 ore generation. *Ore Geol Rev* 30: 181–216

1218

1219 Voudouris P, Melfos V, Moritz R, Spry PG, Ortelli M, Kartal, T (2010) Molybdenite
1220 occurrences in Greece: Mineralogy, geochemistry and rhenium content. In
1221 Christofides G, Kantiradis N, Kostopoulos DS, Chatziperos AA (eds) *Proceedings of*
1222 *the XIX Congress of the Carpathian Balkan Geological Association. Scientific Annals*
1223 *of the School of Geology, Thessaloniki, Greece: 369–378*

1224

1225 Voudouris P, Melfos V, Spry PG, Kartal T, Schleicher H, Moritz R, Ortelli M (2013a)

1226 The Pagoni Rachi/Kirki Cu-Mo±Re±Au deposit, northern Greece: Mineralogical and

1227 fluid inclusion constrains on the evolution of a telescoped porphyry-epithermal

1228 system. *Can Mineral* 51: 411–442

1229

1230 Voudouris P, Melfos V, Spry PG, Bindi L, Moritz R, Ortelli M, Kartal T (2013b)

1231 Extremely Re-rich molybdenite from porphyry Cu-Mo-Au prospects in northeastern

1232 Greece: Mode of occurrence, causes of enrichment, and implications for gold

1233 exploration. *Minerals* 3: 165–191

1234

1235 Wasserburg G, Jacousen S, DePaolo D, McCulloch M, Wen T (1981) Precise

1236 determination of Sm/Nd ratios, Sm and Nd isotopic abundances in standard

1237 solutions. *Geochim Cosmochim Acta* 45: 2311–2323

1238

1239 Whitney DL, Bozkurt E (2002) Metamorphic history of the southern Menderes massif,

1240 western Turkey. *Bull Geol Soc Am* 114: 829–838

1241

1242 Winchester JA, Floyd PA (1977) Geochemical discrimination of different magma

1243 series and their differentiation products using immobile elements. *Chem Geol* 20:

1244 325–343

1245

1246 Yiğit Ö (2006) Gold in Turkey — a missing link in Tethyan metallogeny. *Ore Geol*

1247 *Rev* 28: 147–179

1248

1249 Yiğit Ö (2009) Mineral deposits of Turkey in relation to Tethyan metallogeny:
1250 implications for future mineral exploration. *Econ Geol* 104: 19–51
1251

1252 Yilmaz Y (1989) An approach to the origin of young volcanic rocks of western Turkey.
1253 In: Şengör AMC (ed), *Tectonic evolution of the Tethyan region. SE - 10, NATO ASI*
1254 *Series. Springer: 159–189*
1255

1256 Zartman RE, Doe BR (1981) Plumbotectonics — the model. *Tectonophysics* 75:
1257 135–162
1258

1259 Zhao JH, Zhou MF (2007) Geochemistry of Neoproterozoic mafic intrusions in the
1260 Panzhihua district (Sichuan Province, SW China): Implications for subduction-related
1261 metasomatism in the upper mantle. *Precambrian Res* 152: 27-47
1262

1263 Zindler A, Hart S (1986) Chemical Geodynamics. *Annu Rev. Earth Planet Sci* 14:
1264 493–571
1265
1266
1267

1268 **Figure Captions**

1269 **Fig. 1** Simplified regional tectonic-geological map of western Anatolia and location of
1270 the Pınarbaşı Mo-Cu prospect and major ore deposits/prospects related with the
1271 main tectonic structures in western Anatolia (modified after [Dilek et al. 2009](#); [Öner
1272 and Dilek 2011](#)). Inset shows main plate boundaries, major suture zones,
1273 metamorphic massifs and tectonic units of the Aegean and eastern Mediterranean
1274 region (modified after [Dilek 2006](#); [Dilek and Sandvol 2009](#); [Okay and Tüysüz 1999](#))
1275 BFZ: Bornava flysch zone; CACC: Central Anatolian Crystalline Complex; EAFZ:
1276 East Anatolian fault zone; EF: Eceemis fault; KA: Kazdağ massif; IASZ: Izmir–Ankara
1277 suture zone; ITSZ: Inner–Tauride suture zone; MM: Menderes massif; NAFZ: North
1278 Anatolian fault zone.

1279
1280 **Fig. 2 a** Simplified geological map of the Pınarbaşı (Gediz) prospect ([Delibaş et al.
1281 2012a, b](#)), inset shows location of the Pınarbaşı Mo-Cu prospect within the
1282 Erdoğmuş-Yenigediz graben (modified after [Gürboğa et al. 2013](#)), **b** generalized
1283 stratigraphic column of the study area (modified after [Akdeniz and Konak 1979](#);
1284 [Delibaş et al. 2012a, b](#))

1285
1286 **Fig. 3** Field relationships at the Pınarbaşı prospect. **a** EW-trending normal fault
1287 system cutting monzonite and associated silicified zones, **b** NE-trending late stage
1288 normal fault cutting supergene argillic alteration zones, **c** contact relationships
1289 between monzonite and limestone, **d** magnetite-epidote-pyroxene skarn zones along
1290 contacts of a NW-trending porphyritic granite dyke with ultramafic rocks of the
1291 ophiolitic mélangé unit, **e** drill core sample showing porphyritic granite crosscutting

1292 monzonite, **f** intrusion breccia formed during emplacement of porphyritic granite into
1293 monzonite

1294

1295 **Fig. 4** Different mineralization types at the Pınarbaşı prospect. **a** Pyrite-molybdenite
1296 and chalcopyrite-bearing stockwork quartz-limonite veins crosscutting monzonite with
1297 intense sericitic alteration and stockwork-type mineralization crosscut by late stage
1298 strike-slip and normal fault systems, **b** NE and EW-striking quartz-
1299 molybdenite±chalcopyrite veins crosscutting porphyritic granite, **c** drill core sample
1300 with quartz-molybdenite vein surrounded by sericitic alteration, **d** molybdenite-
1301 bearing intensely silicified zone, **e** drill core sample consisting of a quartz-
1302 molybdenite-pyrite-chalcopyrite vein (Qz: quartz, Py: pyrite, Ccp: chalcopyrite, Mol:
1303 molybdenite, Lm: limonite)

1304

1305 **Fig. 5** Alteration styles and alteration minerals from the Pınarbaşı prospect. **a**
1306 Magnetite veins crosscutting porphyritic granite, **b** K-feldspar vein crosscutting
1307 porphyritic granite, **c** biotite replaced by sericite around quartz-molybdenite veins, **d**
1308 muscovite within sericitic alteration zones, **e** fibroradial pyrophyllite crystals within the
1309 advanced argillic alteration zone, **f** tabular alunite crystals within the advanced argillic
1310 alteration zone (Qz: quartz, Bt: biotite, Ser: sericite, Ms: muscovite, Prl: pyrophyllite,
1311 Alu: alunite)

1312

1313 **Fig. 6** Geochemical classification and discrimination diagrams including magmatic
1314 rock samples from the Pınarbaşı prospect. **a** SiO₂ (wt.%) versus Na₂O+K₂O (wt.%)
1315 classification diagram (Middlemost 1994), **b** AFM plot of **Irvine and Baragar (1971)**,
1316 A: Na₂O+K₂O (wt.); F: FeO_t (wt.); M: MgO (wt.), **c** K₂O (wt.) versus SiO₂

1317 (wt.%) diagram for the samples of Pınarbaşı granitoid (discrimination lines separating
1318 the tholeiitic, calc-alkaline, high-K calc-alkaline and shoshonitic series are from
1319 [Peccerillo and Taylor 1976](#)), **d** Al/(Ca+Na+K) versus Al/(Na+K) molar discrimination
1320 diagram (OMG: Oligo-Miocene Granitoids; [Altunkaynak et al. 2012a](#))

1321
1322 **Fig. 7 a** Primitive mantle-normalized ([Sun and McDonough 1989](#)) multi-element
1323 patterns for rock samples from the Pınarbaşı pluton, **b** chondrite-normalized ([Sun
1324 and McDonough 1989](#)) REE patterns for rock samples from the Pınarbaşı pluton
1325 (Upper and Lower Crust data from [Rudnick and Gao 2003](#); data for Menderes Massif
1326 metamorphic rocks from [Çoban et al. 2012](#))

1327
1328 **Fig. 8** Pb, Nd and Sr isotopic compositions of rock samples from the Pınarbaşı pluton
1329 compared with various potential source reservoirs and rocks. The composition of
1330 present-day CHUR was calculated for 20 Ma. Lead isotope Upper Crust and Orogen
1331 curves from [Zartman and Doe \(1981\)](#). BG: Baklan Granitoid ([Aydoğan et al. 2008](#));
1332 BSE: Bulk silicate earth from [Zindler and Hart \(1986\)](#); DMM: Depleted MORB; EM1:
1333 Enriched mantle I; EM2: Enriched mantle II; EMSS: Eastern Mediterranean Sea
1334 Sediments ([Klaver et al. 2015](#)); EOG: Eocene Granitoids ([Altunkaynak et al. 2012b](#));
1335 GLOSS: Global Subducted Sediments ([Plank and Langmuir 1998](#)); KV: Kula volcanic
1336 rocks ([Güleç 1991](#); [Alici et al. 2002](#); [Innocenti et al. 2005](#); [Dilek and Altunkaynak
1337 2010](#); [Chakrabarti et al. 2012](#)); MMM: Menderes Massif metamorphic rocks ([Çoban
1338 et al. 2012](#)); OMG: Oligo-Miocene Granitoids ([Altunkaynak et al. 2012a](#)); SMV: Simav
1339 volcanic-subvolcanic rocks ([Çoban et al. 2012](#))

1340

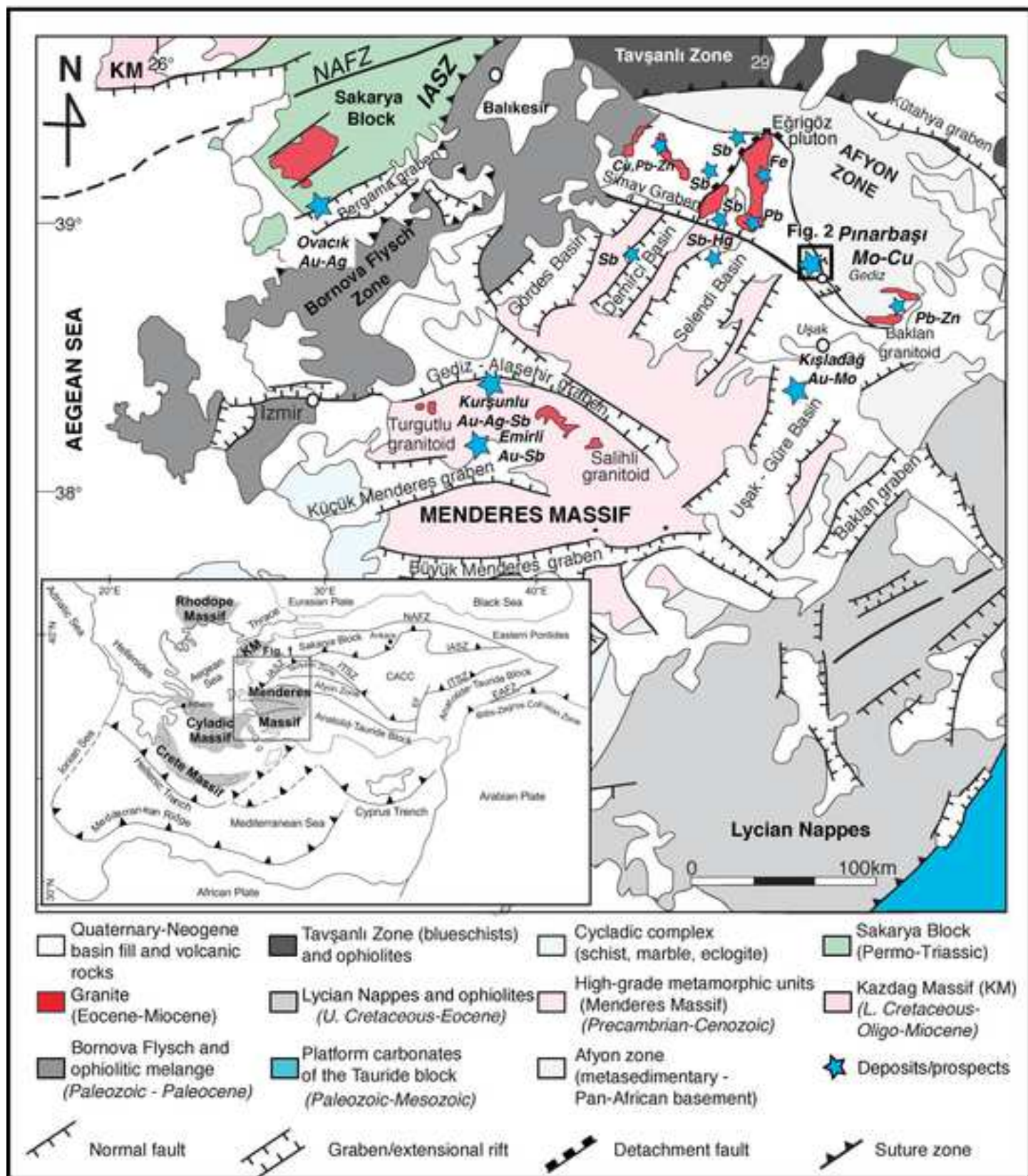
1341 **Fig. 9** Trace element and isotope variation diagrams for magmatic rocks from the
1342 Pınarbaşı pluton: **a** Dy/Yb versus SiO₂ (wt.%), **b** Zr/Sm versus SiO₂ (wt.%) ,**c** initial
1343 ⁸⁷Sr/⁸⁶Sr versus 1/Sr (1/ppm), **d** SiO₂ (wt.%) versus initial ²⁰⁸Pb/²⁰⁴Pb isotope ratios
1344 (AFC: assimilation + fractional crystallization trend from DePaolo 1981)

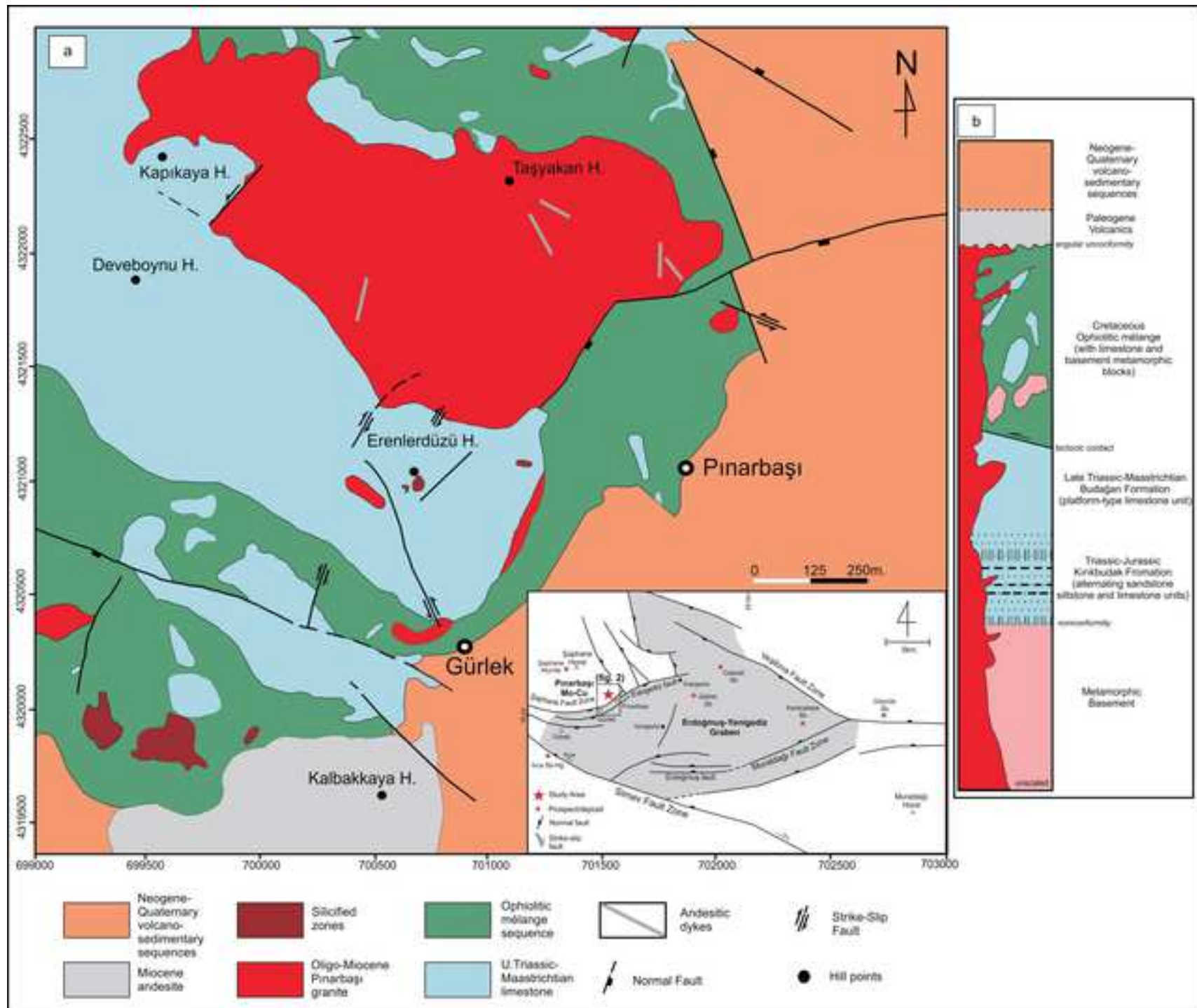
1345
1346 **Fig. 10** **a** (Na₂O+K₂O+Fe₂O₃+MgO+TiO₂) versus Na₂O+K₂O)/(Fe₂O₃+MgO+TiO₂)
1347 discrimination plot for granite melt sources (Patiño Douce 1999), **b** La (ppm) versus
1348 La/Yb diagram, with partial melting and fractional crystallization trends from Thirlwall
1349 et al. (1994), **c** La/Sm versus Sm/Yb diagram, with pressure-dependent pyroxene
1350 and amphibole stabilities from Kay and Mpodozis (2001), **d** Nb–Y–Ga*3 granite
1351 classification diagram after Eby (1992). BG: Baklan granitoid (Aydoğan et al. 2008);
1352 EG: Eğrigöz granitoid (Altunkaynak et al. 2012a, Çoban et al. 2012); SMV: Simav
1353 volcanic-subvolcanic rocks (Çoban et al. 2012)

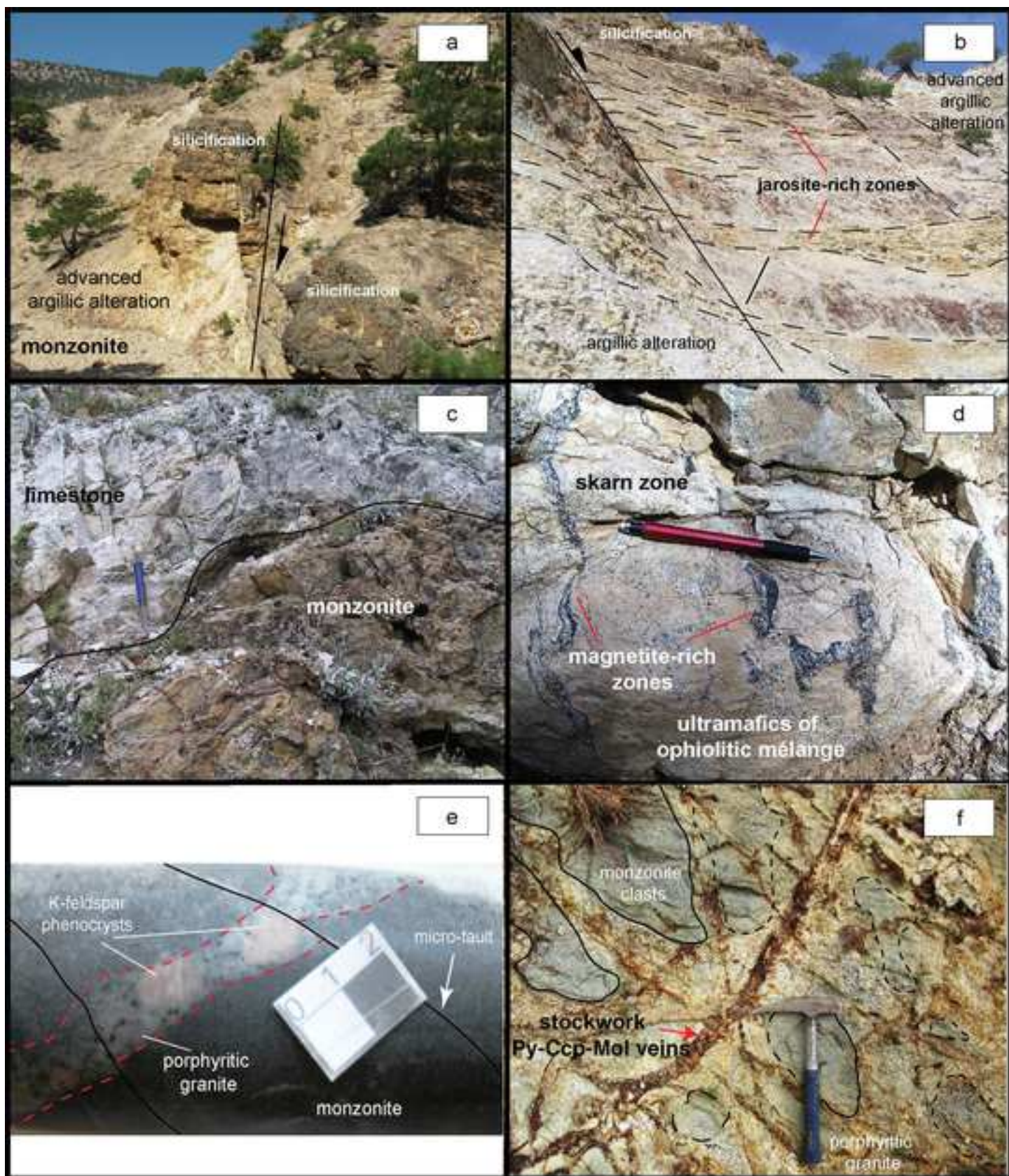
1354
1355 **Fig. 11** **a** Ta/Yb versus Th/Yb discrimination diagram after Pearce (1983), **b** Nb/Yb
1356 versus Ba (ppm) diagram, **c** Nb/Y versus Rb/Y diagram, fluid- and melt-related
1357 enrichment trends from Zhao and Zhou (2007), **d** Ba/Th versus Th/Nb diagram, **e**
1358 Ba/La versus Th/Yb diagram, **f** Th/Nb versus Ba/Nb diagram with sediment melt and
1359 aqueous fluids trends from Ribeiro et al. (2013). MORB data from Hofmann (1997).
1360 BG: Baklan granitoid (Aydoğan et al. 2008); EG: Eğrigöz granitoid (Altunkaynak et al.
1361 2012a, Çoban et al. 2012); EMSS: Eastern Mediterranean Sea Sediments (Klaver et
1362 al. 2015); GLOSS: Global Subducted Sediments (Plank and Langmuir 1998)

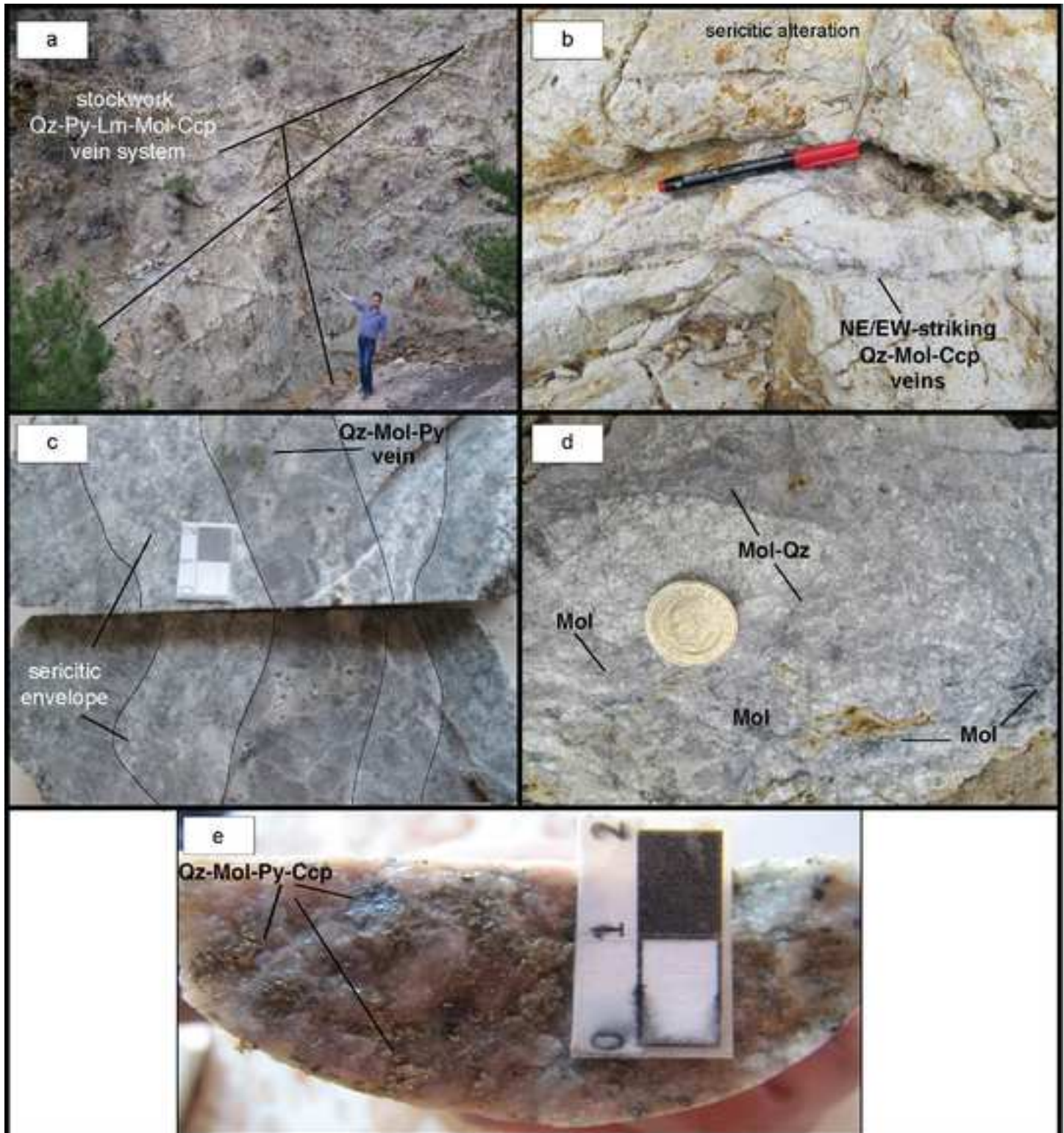
1363
1364 **Fig. 12** Summary of major tectonic and magmatic events within western Anatolia
1365 from Oligocene to Miocene. 1: Jolivet and Brun (2010), van Hinsbergen (2010),

1366 Jolivet et al. (2015); 2-3: Spakman et al. (1988), Jolivet and Brun (2010), van
1367 Hinsbergen (2010), Erkül et al. (2013), Ersoy and Palmer (2013), Jolivet et al. (2013,
1368 2015); 4: Yilmaz (1989), Bozkurt et al. (1993), Hetzel et al. (1995), Bozkurt and Park
1369 (1997), Ring et al. (1999, 2010), Koçyiğit et al. (2000), Whitney and Bozkurt (2002),
1370 Bozkurt and Sözbilir (2004), Dilek et al. (2009), Agostini et al. (2010); 5: Isik et al.
1371 (2004), Ring and Collins (2005), Aydoğın et al. (2008), Hasözbek et al. (2010),
1372 Altunkaynak et al. (2012a); 6: Dilek et al. (2009), Altunkaynak et al. (2012a); 7:
1373 Doglioni et al. (2002), Innocentini et al. (2005), Agostini et al. (2007, 2010), Helvacı et
1374 al. (2009), Karaođlu et al. (2010), Ersoy and Palmer (2013)
1375

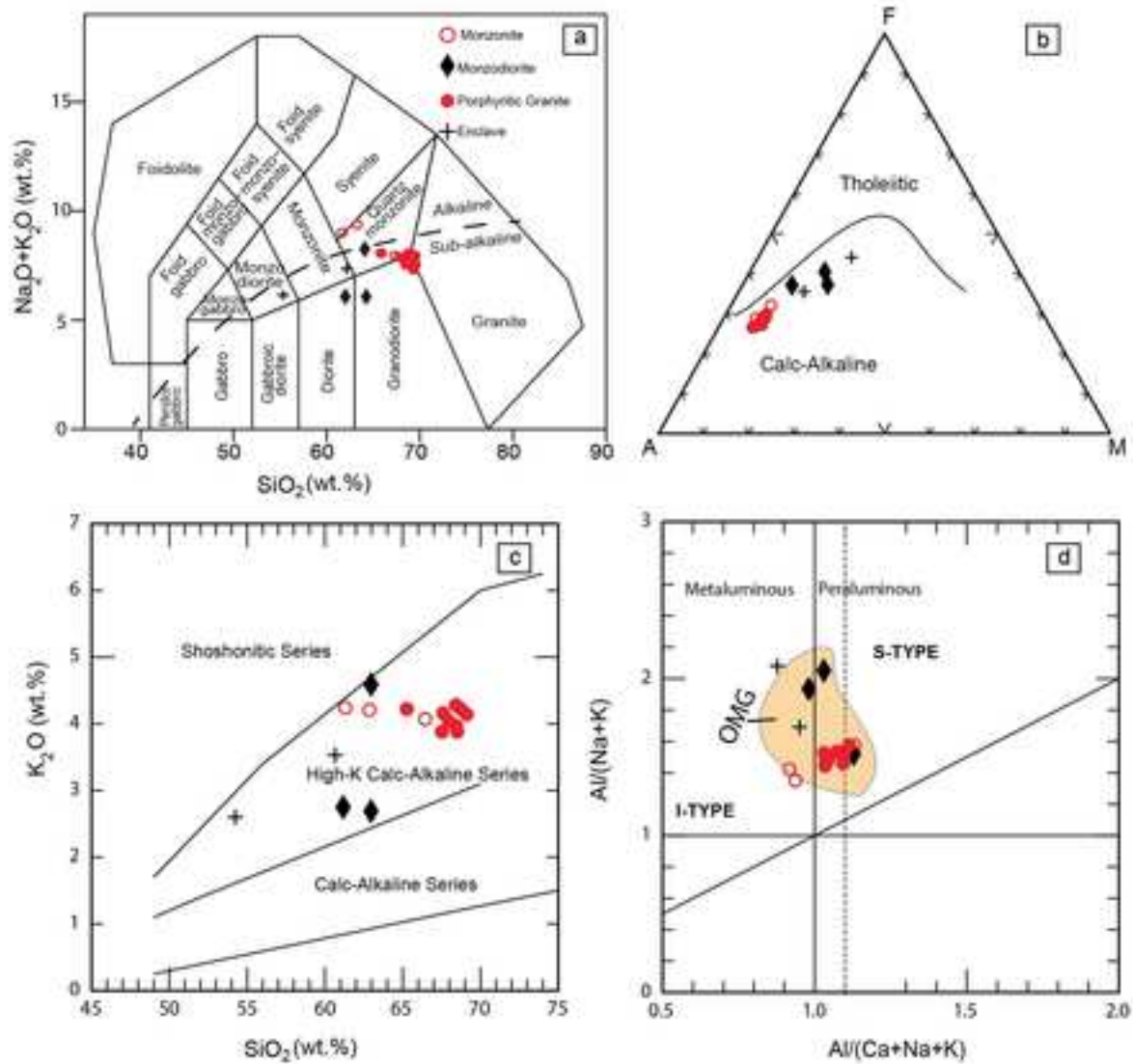


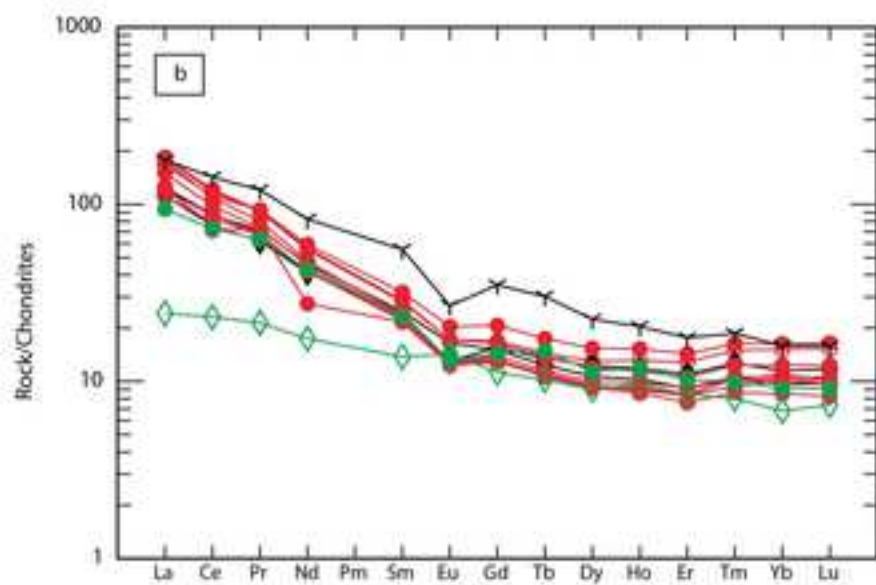
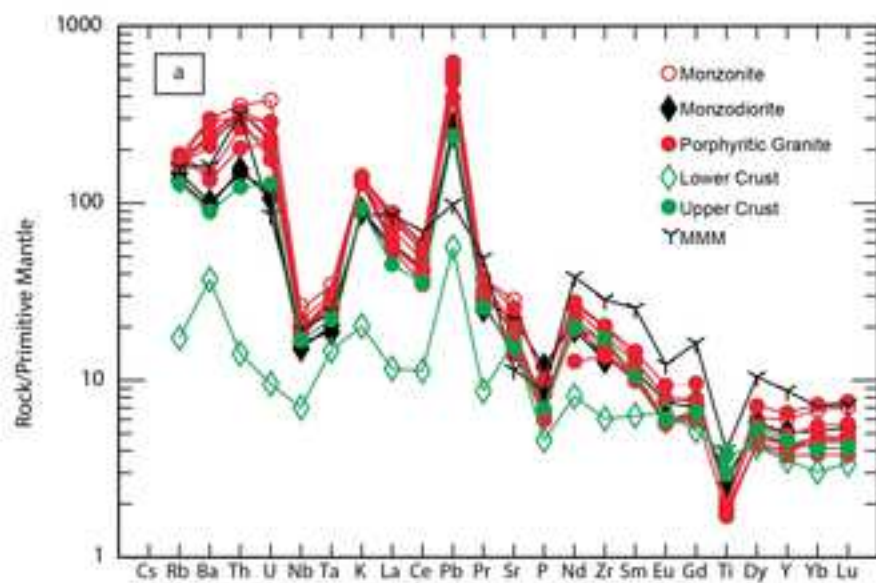


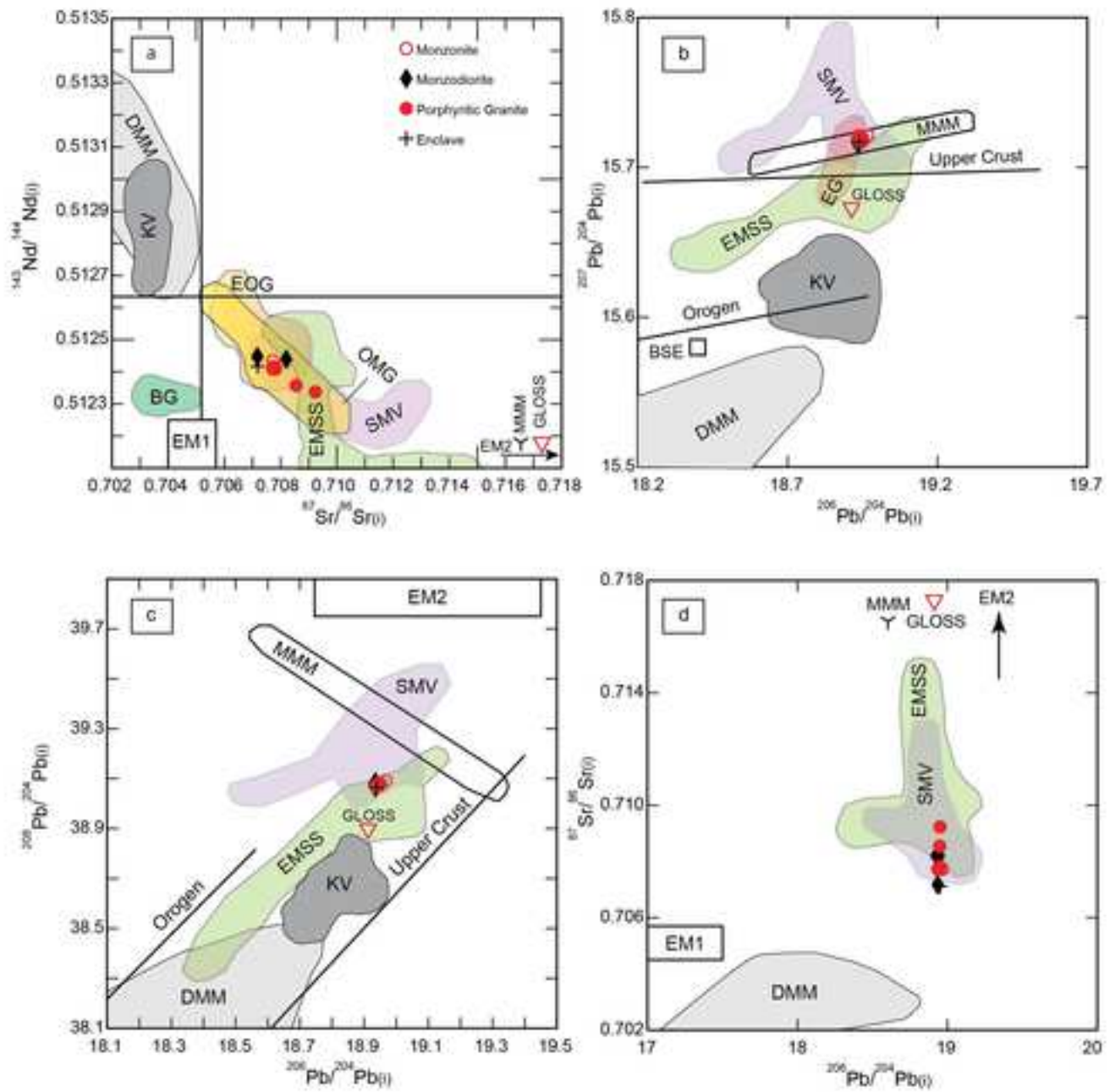


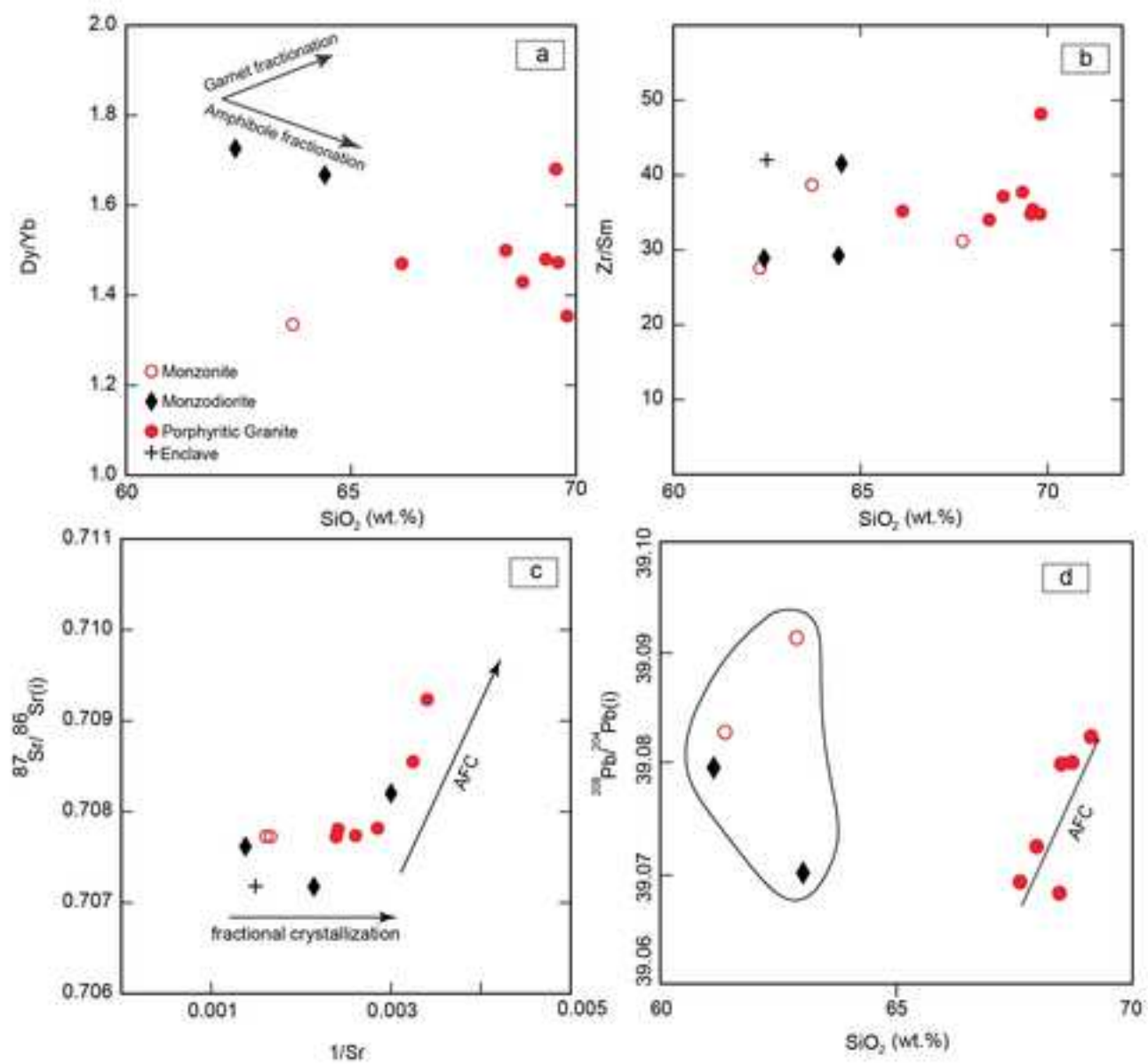


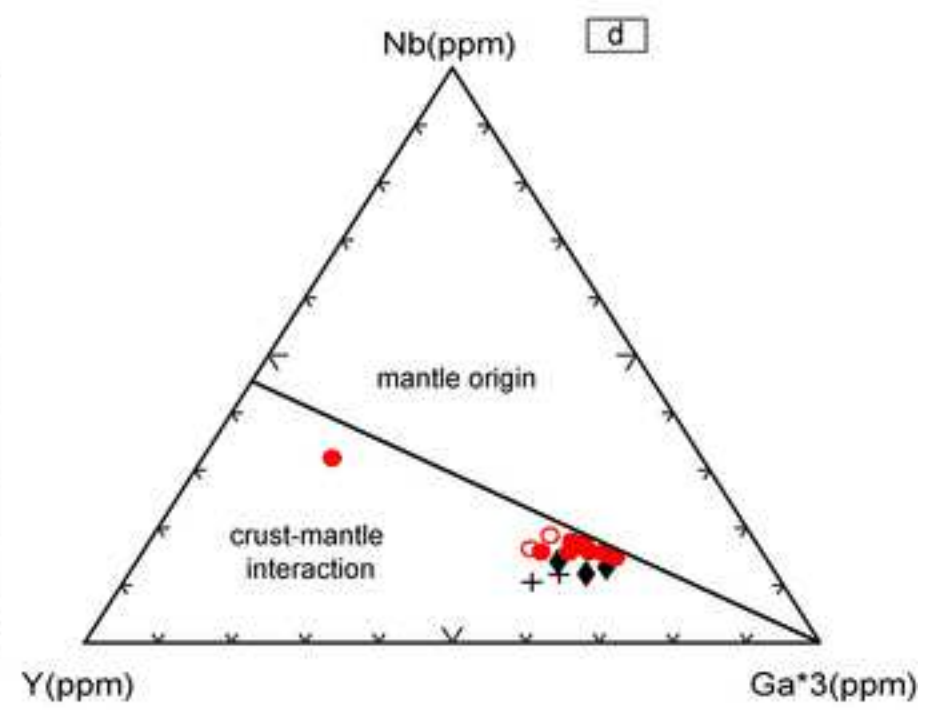
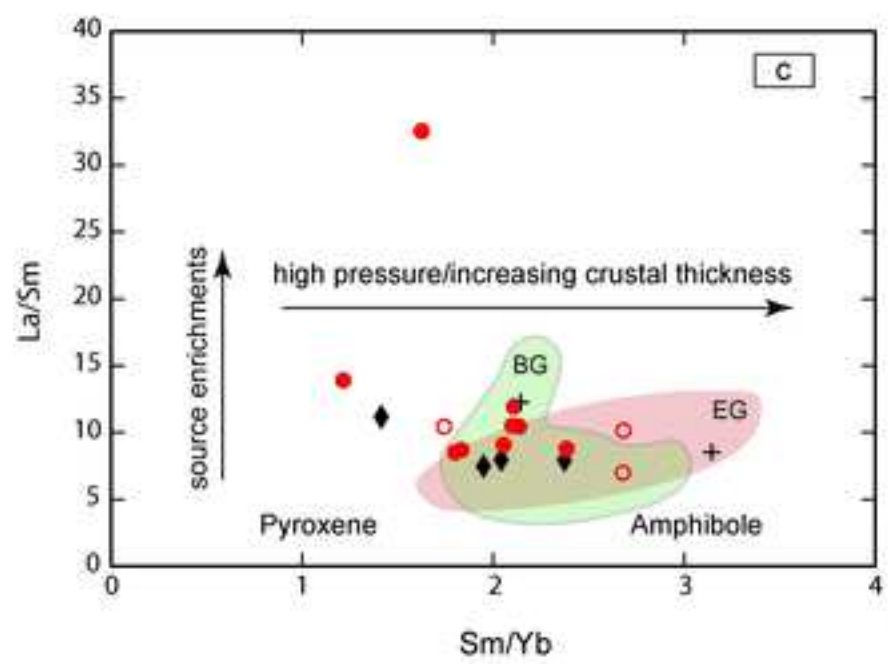
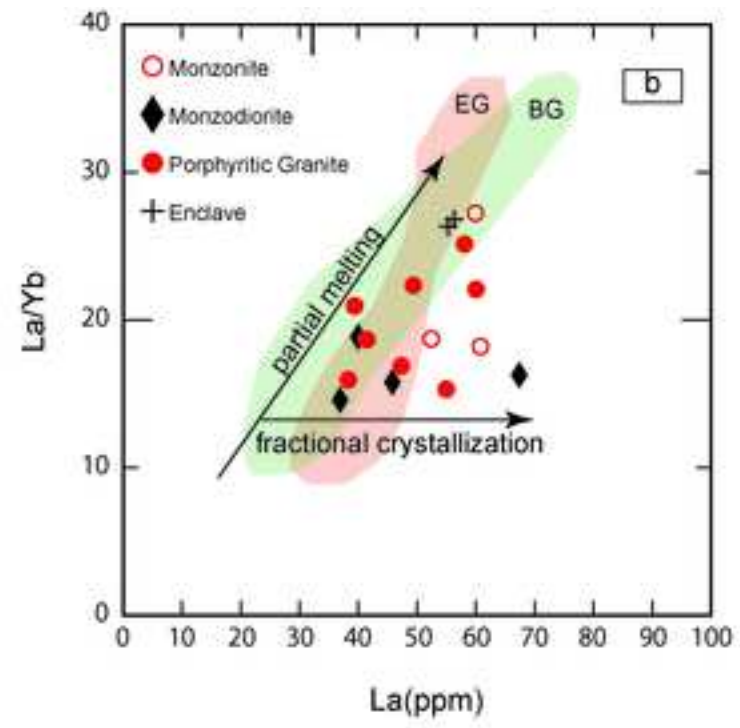
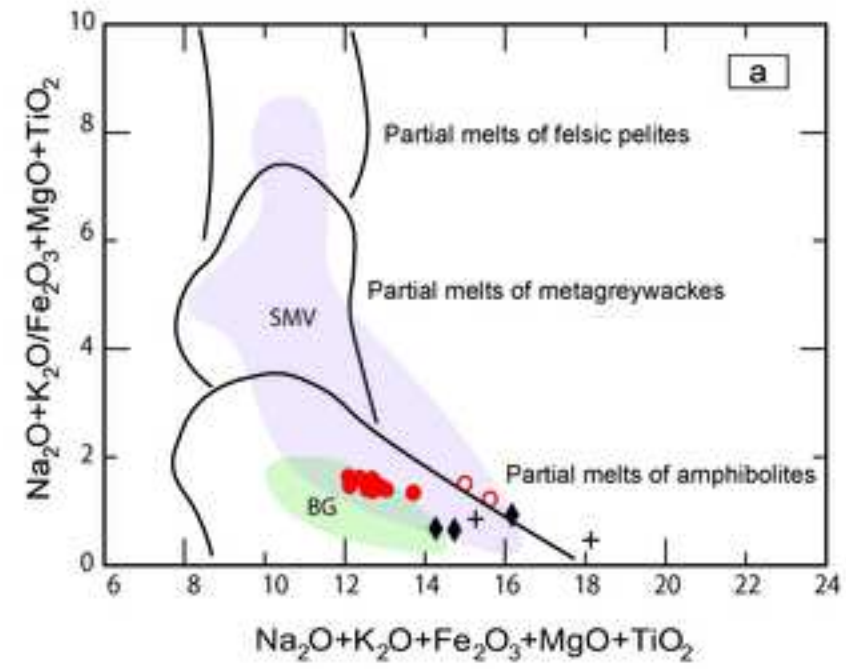


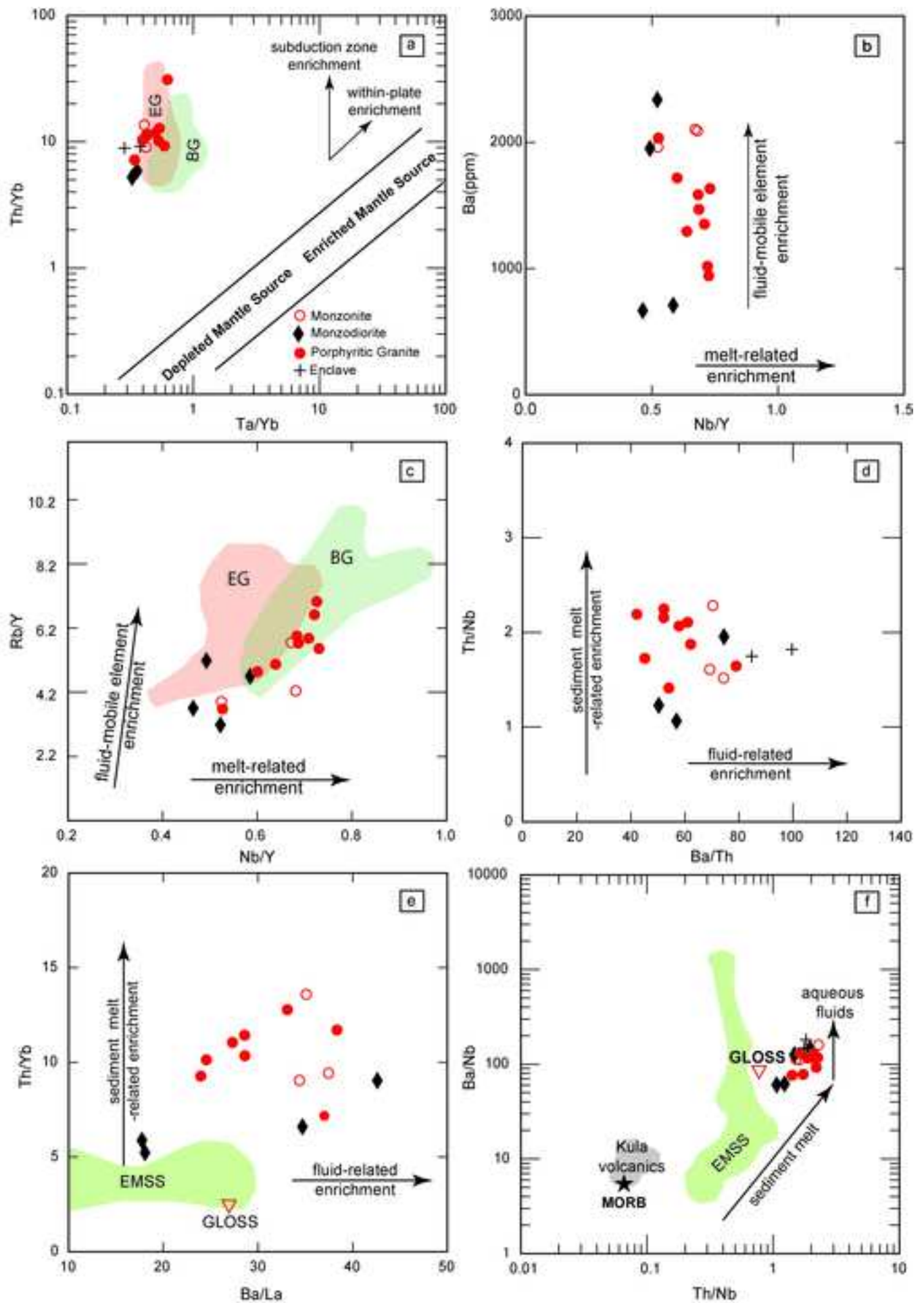












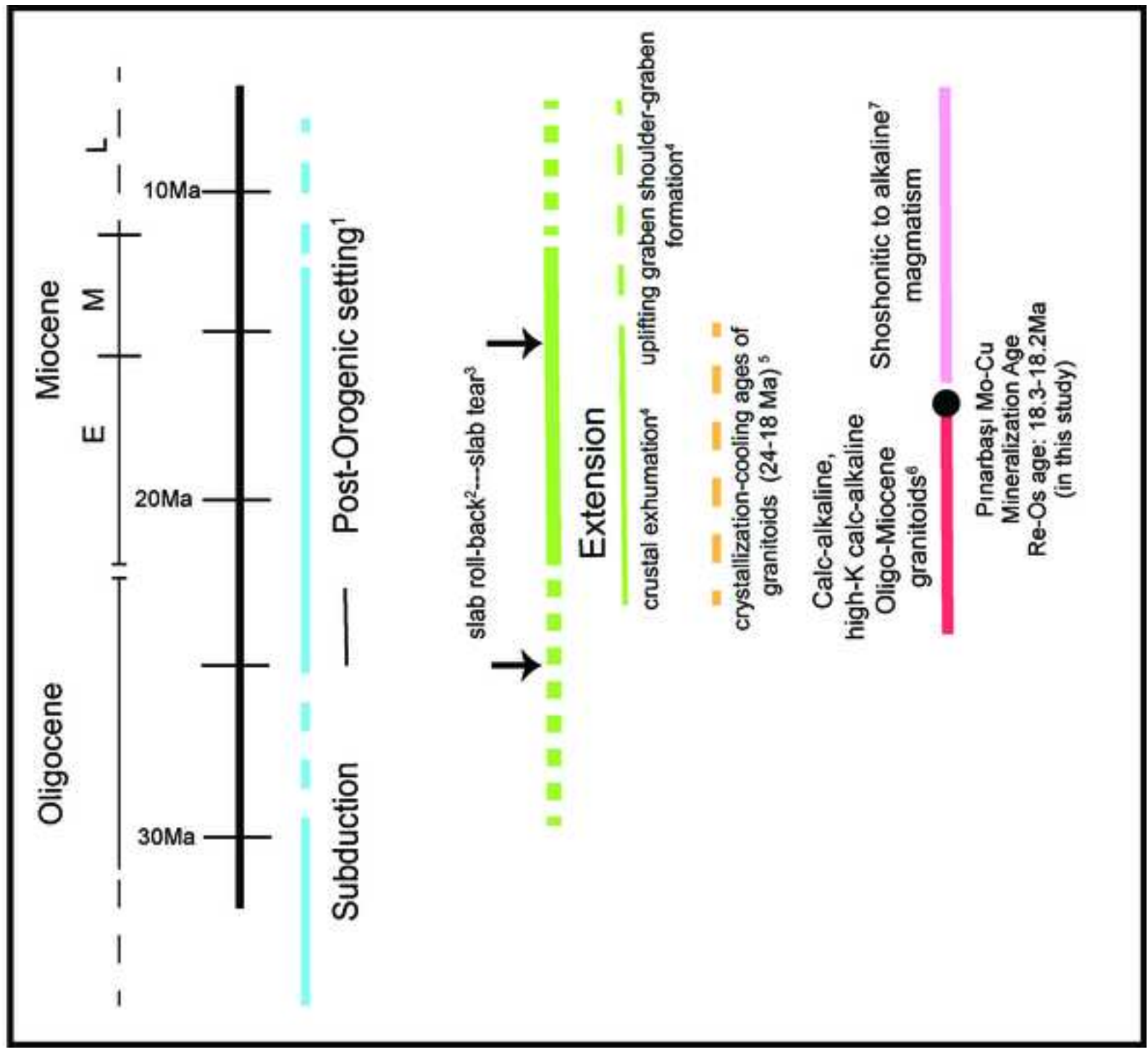


Table 1 Isotope data (Sr and Nd) of magmatic whole rock samples from the Pınarbaşı intrusion.

Sample No	⁸⁷ Sr/ ⁸⁶ Sr	Rb (ppm)	Sr (ppm)	⁸⁷ Sr/ ⁸⁶ Sr(i)	¹⁴³ Nd/ ¹⁴⁴ Nd	Sm (ppm)	Nd (ppm)	¹⁴³ Nd/ ¹⁴⁴ Nd(i)	enD
GOTK1	0.70790	130	621	0.70773	0.51244	7.5	28.9	0.51241	-3.9
GOTK2	0.70789	117	602	0.70787	0.51245	5.8	35.6	0.51243	-3.5
GOTK9	0.70734	94	467	0.70718	0.51246	5.0	29.3	0.51245	-3.2
GOTK11	0.70799	118	384	0.70774	0.51243	4.9	30.3	0.51242	-3.8
GOTK6	0.70887	120	308	0.70855	0.51237	4.6	26.4	0.51236	-5.0
GOTK12	0.70775	113	724	0.70762	0.51230	8.5	47.6	0.51228	-6.5
GOTK13	0.70801	104	415	0.70781	0.51242	4.7	28.4	0.51241	-4.0
GOTK14	0.70841	86	333	0.70820	0.51245	4.9	26.0	0.51244	-3.4
GOTK15	0.70957	119	294	0.70923	0.51235	4.5	26.4	0.51234	-5.4
GOTK7	0.70805	105	369	0.70782	0.51243	4.5	27.5	0.51241	-3.9
GOTK16	0.70794	108	418	0.70773	0.51242	5.7	34.8	0.51241	-4.0
GOTK3	0.70735	118	591	0.70718	0.51245	3.9	27.0	0.51244	-3.4

Note: enD values are calculated relative to CHUR with present day values of $(^{143}\text{Nd}/^{144}\text{Nd})_{\text{chur}} = 0.512638$ and $^{147}\text{Sm}/^{144}\text{Nd} = 0.1967$, $\lambda^{147}\text{Sm} = 6.54 \times 10^{-12}$ enD: $((^{143}\text{Nd}/^{144}\text{Nd})_{\text{sample}} / (^{143}\text{Nd}/^{144}\text{Nd})_{\text{CHUR}} - 1) \times 10,000$ (Wasserburg et al. 1981; Jacobsen and Wasserburg 1984). Initial values are calculated for an assumed age of 20 Ma.

Table 2 Isotope data (Pb) of magmatic whole rock samples from the Pınarbaşı intrusion.

Sample No	206/204Pb	207/204Pb	208/204Pb	Pb ppm	U ppm	Th ppm	206Pb/Pb204(i)	207Pb/204Pb(i)	208Pb/204Pb(i)
GOTK01	18.992	15.719	39.126	40.5	9.2	26.4	18.946	15.717	39.083
GOTK02	19.001	15.723	39.139	41.5	7.0	30.0	18.967	15.721	39.091
GOTK09	18.961	15.719	39.122	19.6	2.5	12.5	18.935	15.718	39.080
GOTK12	19.044	15.725	39.124	49.6	5.7	27.3	19.021	15.724	39.088
GOTK14	18.961	15.717	39.121	17.3	2.2	13.2	18.935	15.716	39.070
GOTK06	18.975	15.721	39.124	34.0	4.4	22.5	18.949	15.720	39.080
GOTK07	18.977	15.721	39.138	34.1	5.0	28.7	18.948	15.720	39.082
GOTK11	18.969	15.718	39.129	27.8	3.7	25.5	18.942	15.717	39.068
GOTK13	18.984	15.721	39.139	28.1	4.9	28.2	18.949	15.719	39.073
GOTK15	18.976	15.719	39.111	37.2	4.6	17.4	18.951	15.718	39.080
GOTK16	18.959	15.722	39.116	39.8	4.6	28.1	18.936	15.721	39.069
GOTK3	18.976	15.719	39.111	43.0	8.0	30.2	18.939	15.717	39.065

Table 3 Re-Os data for molybdenite from the Pınarbaşı prospect

Sample No	wt (g)	Re (ppm) $\pm 2\sigma$	^{187}Re (ppm) $\pm 2\sigma$	^{187}Os (ppb) $\pm 2\sigma$	Age (Ma) $\pm 2\sigma$ (1)	Age (Ma) $\pm 2\sigma$ (2)
GOP-19m	0.01047	950.3 \pm 4.7	597.3 \pm 3.0	181.2 \pm 0.8	18.21 \pm 0.07	18.21 \pm 0.09
OKY3-4	0.01014	1035.5 \pm 5.2	650.8 \pm 3.3	198.5 \pm 0.9	18.30 \pm 0.07	18.30 \pm 0.09

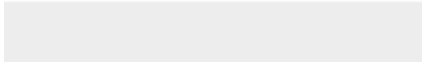
Re-Os dates are calculated using Re decay constants from Smoliar et al. (1996)

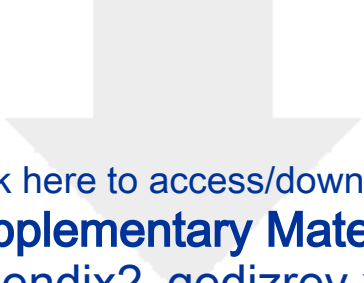
(1) age uncertainty includes all sources of analytical uncertainty

(2) age uncertainty includes all sources of analytical uncertainty and that of the decay constant.

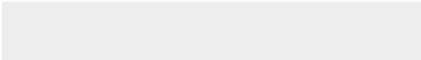
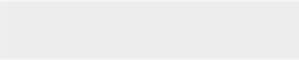


Click here to access/download
Supplementary Material
Appendix1-gediz.docx



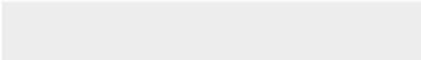
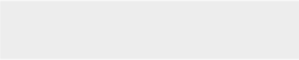


Click here to access/download
Supplementary Material
appendix2_gedizrev.xlsx





Click here to access/download
Supplementary Material
appendix3_Gedizrev.xlsx





Click here to access/download
Supplementary Material
appendix4 NEW.jpg

